Journal of Building Engineering 114 (2025) 114390

Contents lists available at ScienceDirect

Journal of Building Engineering

journal homepage: www.elsevier.com/locate/jobe

Performance and sustainability improvements in foamed lightweight concrete using CRS-activated GGBS binder

Zhi Ge [a], Tianming Gao [a], Hongzhi Zhang [a,*], Faliang Gao [a], Qingyuan Yang [b], Xiaoyu He [c], Branko Šavija [d]

[a] School of Qilu Transportation, Shandong University, Jinan, 250002, China
[b] JiQing High Speed Railway Co., Ltd, Jinan, 250100, China
[c] Shuifa Technology Group Co., Ltd, Jinan, 250100, China
[d] Microlab, Faculty of Civil Engineering and Geosciences, Delft University of Technology, Stevinweg 1, 2628, CN Delft, the Netherlands

ARTICLE INFO

Keywords:
Foamed lightweight concrete
Ground granulated blast furnace slag (GGBS)
Carbide residue slag
Pore structure
Life cycle assessment (LCA)

ABSTRACT

The extensive use of Ordinary Portland cement (OPC) in foamed lightweight concrete (FLC) contributes significantly to its carbon footprint. Concurrently, the disposal of industrial by-products carbide residue slag (CRS) and ground granulated blast furnace slag (GGBS) poses challenges. This study developed a sustainable foamed lightweight concrete system employing CRS-activated GGBS as a complete OPC substitute to address both engineering performance and environmental concerns. An optimal CRS/GGBS ratio (10/90) was determined for achieving the maximum compressive strength in the binder system. Compared to OPC, the CRS/GGBS binder exhibits remarkably low heat of hydration, enabling safer large-volume placements and effectively mitigating the risk of early-age thermal cracking. The prepared CRS/GGBS foamed concrete has much higher compressive strength than those made with cement due to refined air void structure with increased sphericity and improved flexural strength of the solid matrix. The life cycle assessment demonstrated that CRS/GGBS foamed concrete has the ability to decrease carbon emissions by as much as 80 % when compared to cement foamed concrete. This work establishes CRS/GGBS as a technically viable and environmentally superior binder for foamed lightweight concrete, offering enhanced compressive strength, lower thermal cracking risk, and a reduced carbon footprint compared to conventional cement systems in civil engineering.

1. Introduction

Foamed lightweight concrete (FLC) is a lightweight and porous material possessing densities in the range of 300 and 1650 kg/m^3 [1], which has been extensively utilized in prefabricated structures, insulation components, roadways, backfill engineering and other fields [2–4].

Ordinary Portland cement (OPC) has been the primary binder material used in foamed lightweight concrete so far. However, the production of cement is related to significant resource requirements, energy consumption as well as results in carbon emissions. In general, producing one ton of OPC consumes about 6100 MJ of energy and emits about 0.8–1.0 tons of CO_2 into the environment [5]. For foamed lightweight concrete to develop sustainably and to facilitate the low carbon transition, new low carbon binding materials

* Corresponding author.
E-mail address: hzzhang@sdu.edu.cn (H. Zhang).

https://doi.org/10.1016/j.jobe.2025.114390
Received 31 July 2025; Received in revised form 3 October 2025; Accepted 13 October 2025
Available online 17 October 2025

must be developed.

Ground granulated blast-furnace slag (GGBS) is a valuable by-product that emerges from the iron production process [6]. Numerous studies have been conducted exploring the partial or complete replacement of OPC with GGBS [7–9]. Although GGBS can hydrate on its own, it does so at a relatively slow rate. Generally, to expedite the hydration process of GGBS, chemical activators such as alkaline hydroxides, soluble silicates, and sulfates are utilized [10–12]. The type and dosage of activators play a pivotal role in determining the composition and physical characteristics of the hydration products. Consequently, these factors exert a profound impact on the engineering performance of the GGBS binder [13,14]. However, the use of strong alkalis like sodium hydroxide (NaOH) in GGBS activation presents several practical challenges, including rapid setting times, economic inefficiencies, and the hazards associated with handling materials of high pH [15,16]. Consequently, the application of alkaline earth activators, such as magnesium hydroxide and calcium hydroxide, in GGBS activation has garnered significant interest. This is attributed to their cost-effectiveness and robust activation efficacy [17,18].

Research on alkali-activated slag (AAS) binders, including those utilizing waste-derived activators like carbide residue slag (CRS), has demonstrated their potential as sustainable alternatives to OPC [19]. Carbide residue slag (CRS) is a by-product generated during the production of acetylene [20]. Generally, CRS consists of calcium hydroxide (>80 %), calcium carbonate (<10 %) and minor carbon and silicates [21]. CRS can result in land occupation and environmental pollution if not disposed of correctly [22,23]. Given their similar mineral composition, CRS could potentially replace calcium hydroxide in the activation of GGBS. Studies investigating CRS-activated GGBS systems, often blended with supplementary materials like fly ash (FA), have reported achieving compressive strengths typically in the range of 10–30 MPa [24]. Recent research has further highlighted that the activation efficiency of Ca-based activators on GGBS is strongly dependent on the $Ca(OH)_2$ content and particle size of the activator [16]. However, these investigations have primarily focused on bulk pastes or mortars, with significantly less attention paid to their applicability in lightweight cellular systems like foamed concrete.

The hardened properties of FLC, particularly its thermal insulation efficiency and mechanical strength, are dominantly governed by its unique air-void structure, characterized by pore volume, size distribution, sphericity, connectivity, and wall thickness [25–28]. Optimal performance often requires a finely dispersed, uniform pore structure with minimal interconnection for enhanced mechanical strength, alongside a high proportion of small, closed pores for superior insulation [29]. While substantial research has been dedicated to characterizing the pore structure of conventional OPC-based FLC, studies focusing on the pore architecture of FLC produced with alternative binders, especially those derived from solid wastes, are remarkably scarce [30].

To this end, this study proposes a foamed lightweight concrete system that employs CRS-activated GGBS as the primary binder. The optimal binder ratio was first determined to maximize performance, and the associated hydration mechanisms were elucidated. Subsequently, a series of FLCs with varying densities were designed and fabricated. The 3D pore structure of these materials was characterized using X-ray computed tomography (X-CT) and then correlated with their mechanical properties. Furthermore, the CO_2 reduction potential was quantitatively evaluated through life cycle assessment (LCA). By enabling the synergistic utilization of solid wastes, this work aims to promote the wider application of sustainable and economical foamed lightweight concrete in civil engineering.

2. Materials and methods

2.1. Materials

Ground granulated blast furnace slag (GGBS) and carbide residue slag (CRS) were used as binder materials. The CRS was dried in a vacuum oven and then grounded before tests. The density of GGBS and grounded CRS is 2900 kg/m^3 and 2185 kg/m^3, respectively.

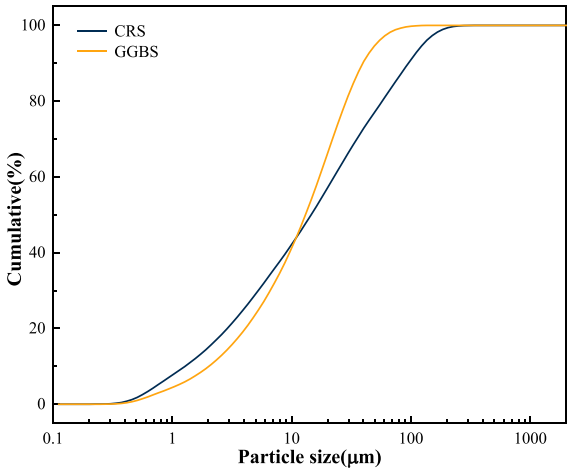

Fig. 1. Particle size distribution of CRS and GGBS.

The particle size distribution of GGBS and CRS measured by laser diffraction particle size analyzer is shown in Fig. 1. Table 1 displays the specific surface area (SSA) and median particle diameter of both GGBS and CRS, providing a detailed comparison of their physical properties. The grounded CRS has larger particles and smaller SSA than GGBS. Table 2 presents the oxide compositions of CRS and GGBS as measured by X-ray diffractometer. CaO occupies 94.35 % of CRS by weight. CaO and SiO_2 account for 37.11 % and 30.49 % of the weight of GGBS, respectively. Fig. 2 shows the XRD spectra of GGBS and CRS. CRS mainly contains Ca $(OH)_2$ and GGBS is mainly composed of a large amount of glassy phase.

2.2. Preparation and characterization of CRS/GGBS paste blends

Both GGBS and CRS were considered as the binder. In order to determine the optimal CRS/GGBS ratio, four mixtures were designed. Their CRS/GGBS ratios were 5/95, 10/90, 15/85, 20/80 respectively. The water/binder ratio for each of the mixtures was 0.50. The CRS and GGBS were firstly mixed using a mixer for 2 min. Distilled water was added and mixed at low speed for 2 min, then mixed at high speed for another 2 min. Afterwards, the fresh mixtures were prepared for further test.

For the compressive strength measurement, 40 mm × 40 mm × 40 mm cubes cured for 3, 7, and 28 days were prepared. The fresh mixtures were poured in mold and vibrated. Cling film was used to seal the specimen. The specimens were demolded and cured in an environmental chamber with 95 % relative humidity and 20 °C temperature until the age for the measurement, following a 24-h sealing period at a temperature of 20 ± 1 °C. Three specimens were tested for each condition, and the average result was determined as the compressive strength. The error bar around each data point is the standard deviation.

For the chemical phases and microstructure characterization, the fresh mixture was first poured into a plastic cylindrical mold (Φ 50 mm × 100 mm) and sealed. The samples were rotated for 24 h to minimize bleeding. Afterwards, they were stored at a temperature of 20 °C under sealed conditions for further analysis. After 7- and 28-days curing, each cylinder was first cut into small pieces with thickness smaller than 1 mm. The hydration was arrested using isopropanol. The samples were then dried in vacuum oven at a temperature of 40 °C until they reached a constant weight.

The X-ray spectra of the powders were obtained by an X-ray diffractometer with Cu-Kα radiation and the samples were scanned in the range of $5° \leq 2\theta \leq 90°$ with a step rate of 2°. Thermogravimetric analysis (TGA) of powders was performed with a resolution of 10 mg. Samples were heated at a rate of 10 °C/min in nitrogen atmosphere from 20 °C to 1000 °C. Fourier transform infrared spectroscopy (FTIR) was conducted using the conventional KBr disc method (1.0 mg of sample to 300.0 mg of KBr). A frequency range of 4000–400 cm^{-1} was scanned.

Isothermal calorimetry (set point 22 °C) was used to assess the hydration of CRS/GGBS blends. The heat evolution was measured with an isothermal calorimeter (CALMETRIX I-CAL 8000HPC). The water/binder ratio used was 0.50 for all mixtures. The fresh mixture was mixed, then poured into a plastic vial and then put inside the calorimeter chamber. The heat evolution rate was continuously monitored and recorded for up to 72 h for the analysis.

2.3. Preparation and characterization of foamed lightweight concrete

2.3.1. Preparation of foamed lightweight concrete

For the preparation of foamed lightweight concrete, the detailed mixture proportions are given in Table 3. The CRS was first initially mixed with water and mixed at 62 rpm for 30 s. GGBS was then incorporated into the mixture, and mixing continued at the same speed for another 60 s. Subsequently, the mixture was stirred at 125 rpm for another 60 s to ensure homogeneity. Prior to foaming, the composite polymer foaming agent was diluted with water at a mass ratio 1:49. The resulting foam, generated by a foaming machine operating at a compressed air pressure of 0.4 MPa and 25 °C, had a density of 40 kg/m^3. Foam was then added to the mixture within 1 min and blended uniformly by stirring at 62 rpm for approximately 120 s. The wet density and flowability of the mixture were first measured, after which the fresh slurry was carefully transferred into molds. The cling films were used to cover the specimens, and they were cured for 48 h at standard condition. After demolded, they were packed with plastic bags and kept at 20 ± 1 °C until testing. The density was determined using 28 day cured specimens. Each specimen was dried in an oven at 60 °C till its weight remained for the measurement.

2.3.2. X-ray computed tomography and image processing

With a source voltage of 150 kV and current of 72 mA, a single cylindrical sample (Φ 50 mm × 150 mm) that had been cured for 28 days was used for microstructure acquisition using a high resolution micro-XCT system (ZEISS Xradia 510 Versa). The sample was rotated from 0° to 360°. A total of 1000 shadow projections with 50 μm pixel size were obtained (1004 × 1024 pixels). An exposure period of 1.2 s was averaged for each projection image. A 25 mm cubic region of interest (ROI) was meticulously selected from the specimen's core for threshold determination. This threshold was then employed to distinguish between the pore and solid phases within the sample, thereby mitigating the effects of beam hardening observed in the X-ray computed tomography (X-CT) scans, as

Table 1
Specific surface area (SSA) and median particle diameter (Dv50) of raw materials.

Material	SSA (m^2/g)	Dv50 (μm)
GGBS	0.683	13.15
CRS	0.599	19.03

Table 2
Chemical composition of GGBS and CRS.

Oxides	CaO	SiO_2	Al_2O_3	MgO	Fe_2O_3	Na_2O	Na_2O	SO_3	Other
GGBS	37.11	30.49	17.33	8.46	1.16	1.06	1.06	2.09	0.38
CRS	94.35	2.75	2.00	0.06	0.22	0.09	0.09	0.35	0.14

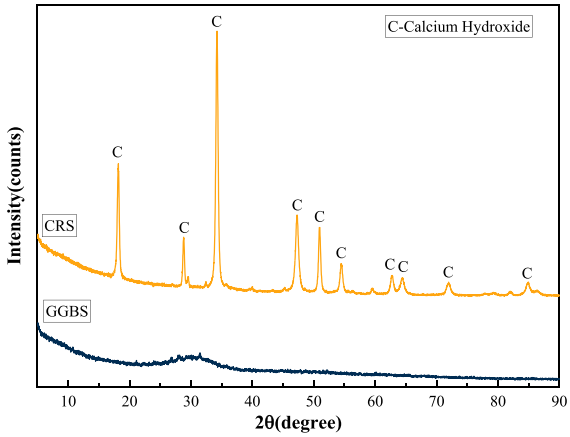

Fig. 2. X-ray spectra of CRS and GGBS.

Table 3
Mixture design of foamed lightweight concrete.

Wet density (kg/m^3)	CRS (kg/m^3)	GGBS (kg/m^3)	Water (kg/m^3)	Foam (kg/m^3)
600	33.78	304.03	236.46	25.73
700	41.00	369.00	266.50	23.50
800	47.93	431.34	299.54	21.19
900	55.07	495.60	330.40	18.94

The compressive strengths at 3, 7, and 28 days were tested using an electronic universal testing machine with a constant loading rate set at 0.5 kN/s. Three specimens for each mixture were tested.

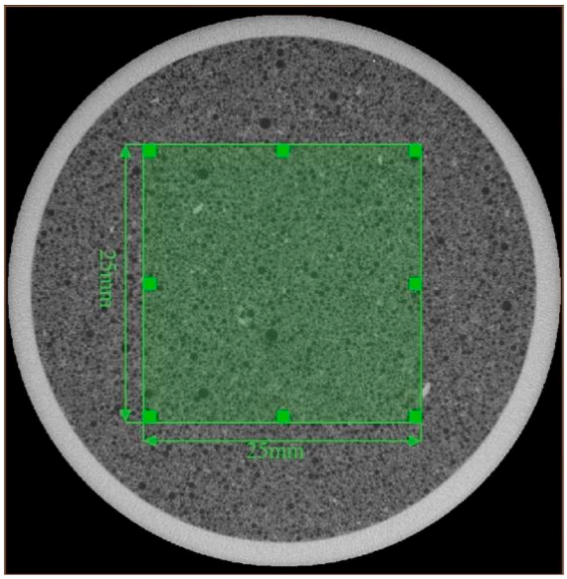

Fig. 3. An example cross sectional XCT image of ROI.

illustrated in Fig. 3. For the sake of simplicity, the foamed lightweight concrete was regarded as a two-phase material consisting of porous phase and hydrated paste phase. The cumulative distribution and logarithmic cumulative distribution of grayscale value were derived and the intersection of the two curves was used as the threshold for the image segmentation, see Fig. 4. Fig. 5 compares the image before and after segmentation of the ROI. The volume ratio between the ROI and pore phase was used to determine the porosity.

2.3.3. Rheology

The rheology of the slurry was assessed using a Brookfield RST-CC rheometer equipped with the CCT-40 coaxial cylinder measurement system. This instrument configuration has shear rate, shear stress, and viscosity ranges of 0.0215–2790 s^{-1}, 0.89–594 Pa, and 0.3–2.7 $\times$ 10^7 mPa s, respectively. For testing, the outer cylinder was fixed, and the sample and rotor were loaded into the cylindrical chamber. The testing software controlled the rotor rotation speed.

Fig. 6 illustrates this testing sequence. Rheological properties were measured for both fresh mixtures with and without foam. Each test began with a constant shear rate applied for 90 s to disrupt the mixture structure and ensure uniform initial conditions. This was followed by a 30-s rest period to allow sample recovery. Subsequently, the shear rate was linearly increased from 0 to 100 s^{-1} (upward sweep) and then decreased from 100 to 0 s^{-1} (downward sweep) to generate flow curves. Yield stress and plastic viscosity were determined by applying the Bingham plastic model to the shear stress-shear rate data collected specifically during the 180–240 s interval of shearing (within the downward sweep phase). This approach was applied to characterize both the fresh paste blends and the foamed lightweight concrete.

In accordance with the Chinese standard JGJ/T 341–2014, the fluidity of the foamed lightweight concrete mixture was evaluated. Fresh mixture was placed into an Φ80mm $\times$ 80 mm cylinder. After allowing it to spread spontaneously for 60 s, the cylinder was lifted. The maximum spread diameter and the vertical diameter of the collapsed concrete mass were measured using a vernier caliper. The fluidity value was calculated as the average of these two measurements.

2.4. Life cycle assessment

The environmental impact of CRS/GGBS and OPC foamed lightweight concrete was analyzed life cycle assessment (LCA) [31,32]. The foamed lightweight concretes mixture with density of 600–900 kg/m^3 were picked for comparison, and their mixture proportions are presented in Table 4.

The LCA mainly consists of four steps: defining the functional unit and system scope, conducting a life cycle inventory analysis (LCI), conducting a life cycle impact assessment (LCIA), and life cycle interpretation. This methodology adheres to the ISO 14040: 2006 standard [33]. For 1 m^3 foamed lightweight concrete, the functional unit and system scope for life cycle were defined as "cradle--to-gate" with Fig. 7 illustrating the key processes [34]. The three main stages of the system are raw material production, transportation, and production of foamed lightweight concrete. Cement was produced in cement plants, GGBS was generated in the steel plant, foam agent was produced in chemical plants, and water was abstracted from a municipal water treatment facility during the raw material production stage. According to the "cut-off" principle, CRS was regarded as waste, and the environmental impact of its "manufacture" was seen as zero [35]. The transportation distances of CRS and GGBS were both set as 200 km. The processes include powder mixing, foam preparation, and the preparation and curing of the foamed lightweight concrete itself are involved in the manufacturing of foamed lightweight concrete. As indicated in Table 5, Tables 6 and 7, the LCI data for each stage were obtained from Chinese Life Cycle Database and relevant literature.

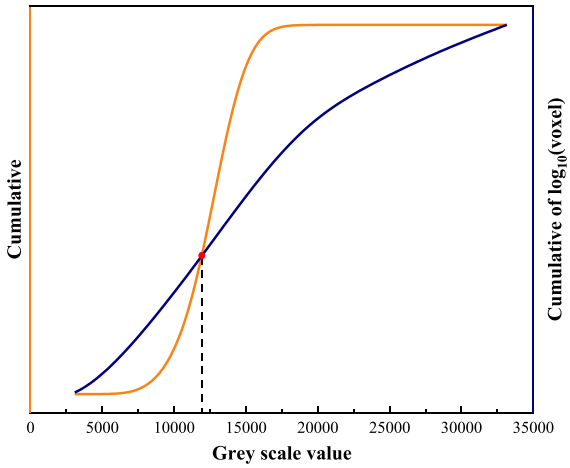

Fig. 4. Determination of thresholds.

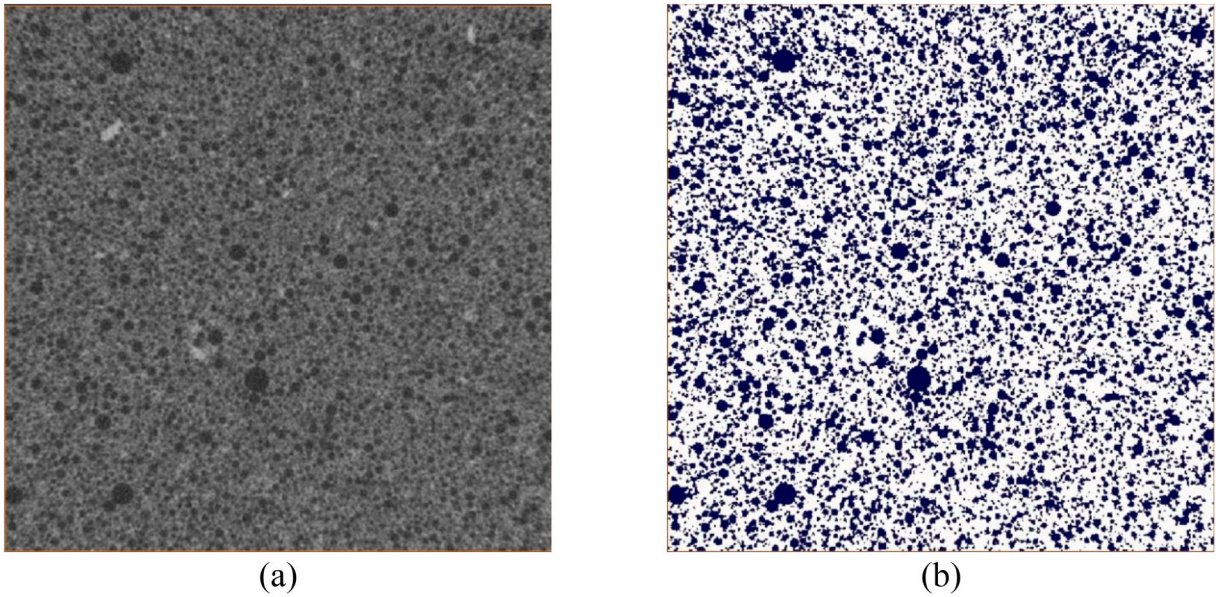

Fig. 5. Comparison of the image before and after image segmentation of the ROI. (a) Original grayscale image; (b) after image segmentation.

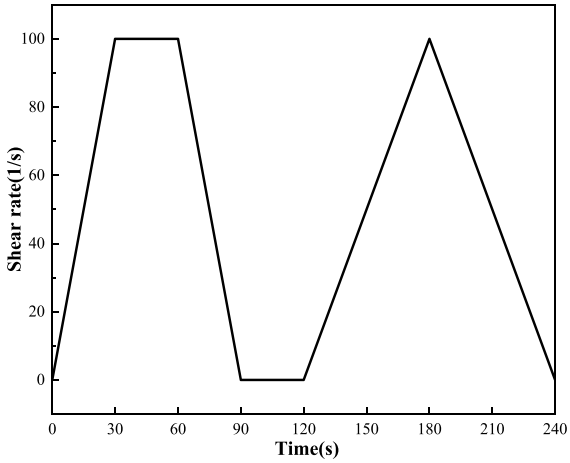

Fig. 6. The testing scheme of rheological behavior.

Table 4
Mixture proportions of OPC and CRS/GGBS foamed lightweight concrete for LCA.

Materials	Cement (kg/m^3)	GGBS (kg/m^3)	CRS (kg/m^3)	Foam agent (kg/m^3)	Total water (kg/m^3)
OPC-600	386.0			0.410	213.090
OPC-700	454.0			0.376	245.424
OPC-800	521.0			0.344	277.856
OPC-900	589.0			0.310	310.190
CRS/GGBS-600		304.03	33.78	0.5146	261.6754
CRS/GGBS-700		369.00	41.00	0.4700	289.5300
CRS/GGBS-800		431.34	47.93	0.4238	320.3062
CRS/GGBS-900		495.60	55.07	0.3788	348.9612

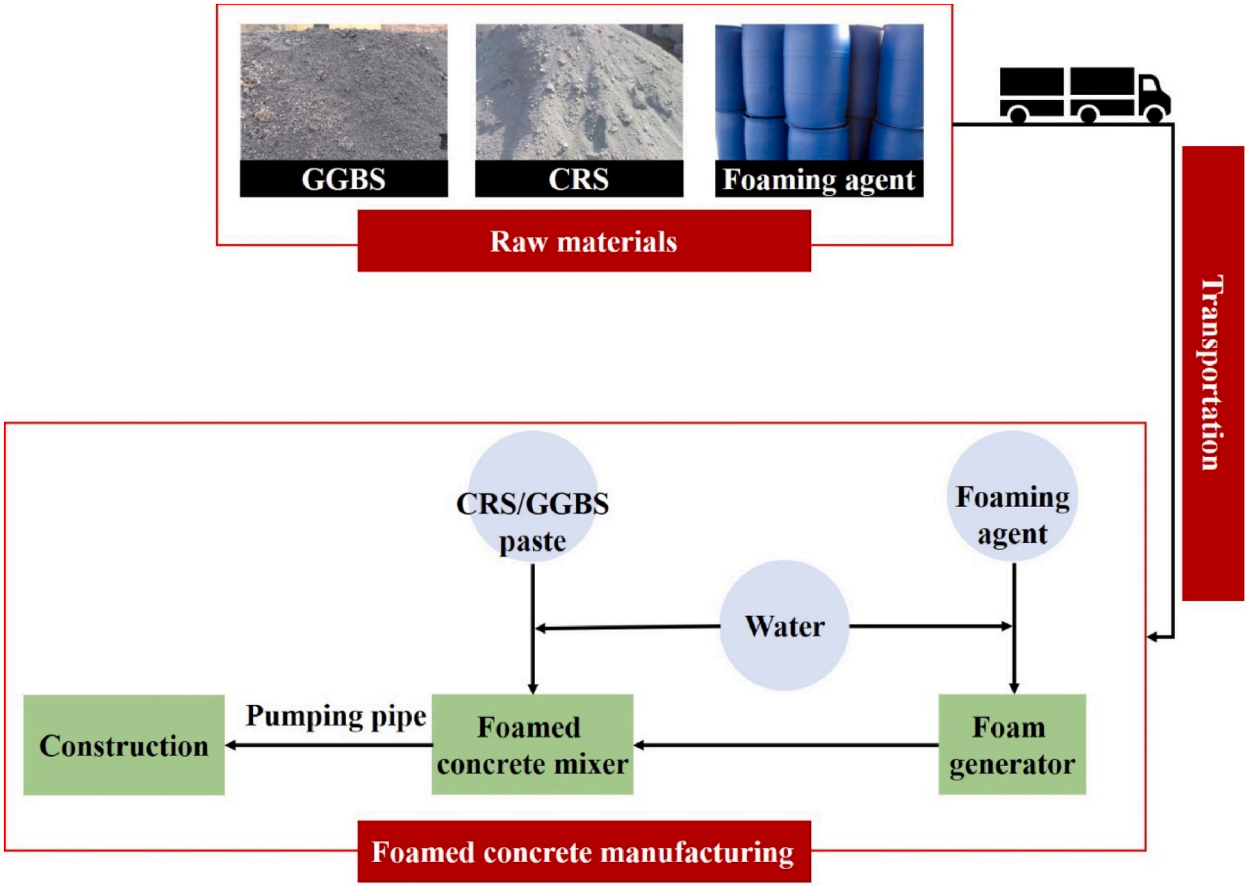

Fig. 7. System scope of life cycle assessment for foamed lightweight concrete.

Table 5
LCI of raw materials and energy derived from Refs. [31,35,36].

Materials	Global Warming Potential	
	Value	Units
Cement	0.726	kg CO_2 eq/kg
GGBS	0.085	kg CO_2 eq/kg
Water	0.000106	kg CO_2 eq/kg
Foaming agent	0.779	kg CO_2 eq/kg
Electricity	0.804	kg CO_2 eq/kWh

Table 6
LCI of transportation.

Materials	Distance (km)	Means of Transport
Cement	161	Light diesel trunk
GGBS	200	GWP: 0.410 kg CO_2 eq/(t·km)
CRS	200	
Foaming agent	849	

3. Results and discussion

3.1. CRS/GGBS paste blends

3.1.1. Strength

The measured compressive strengths are presented in Fig. 8. The compressive strength is the highest when the CRS/GGBS ratio is

Table 7
LCI of foamed lightweight concrete manufacturing.

Foamed concrete manufacturing process	Details	Energy
Foam generating	Foam generator	0.2 kW h/m^3
Foamed concrete mixing	Foamed concrete mixer	2.2 kW h/m^3
Foamed concrete pumping	Pumping machine	0.5 kW h/m^3

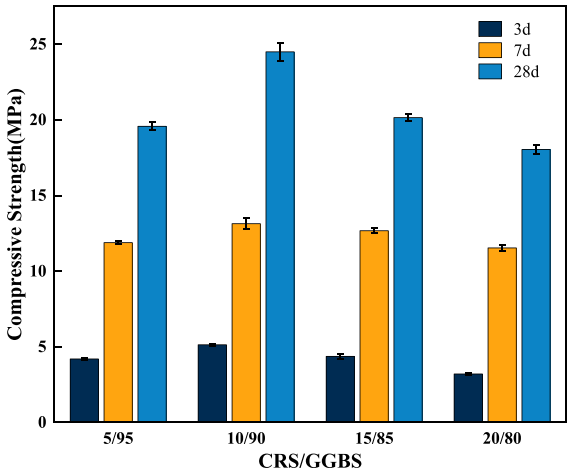

Fig. 8. Influence of CRS/GGBS ratio on the compressive strength at 3, 7 and 28 days.

10/90 for all ages. This optimal CRS/GGBS ratio for compressive strength is in accordance with the observation in Ref. [37]. However, compared with OPC 42.5, the compressive strength of CRS/GGBS mixtures are approximately 65 % and 45 % lower at 7 days and 28 days, respectively [38]. The measured flexural strengths are presented in Fig. 9. The flexural strength of the mixtures exhibits a pattern analogous to that of compressive strength. Mixture with CRS/GGBS ratio of 10/90 has the highest flexural strength of 9.4 MPa which is higher than that of OPC (about 8.9 MPa at 28 days) [38].

3.1.2. Hydration heat

Figs. 10 and 11 show the heat flow and cumulative heat release curve of blends with different CRS/GGBS ratios. Two exothermic peaks appear in all blends. One appears at about 2.8 h and the other at 7 h. They are all related to the formation of C-A-S-H-type gel. The main source of silicate is from GGBS dissolution [39]. As the content of CRS in the blends increases, the exothermic peak appears earlier and the amount of released heat increases. This is due to the dissolution of CRS: the increased alkalinity in the system results in a higher rate of slag reaction, generating more hydration products and releasing more heat. It is worth mentioning that the 3-day cumulative heat of CRS/GGBS blends is about one-third of that of OPC [40]. This could be beneficial in applications where temperature

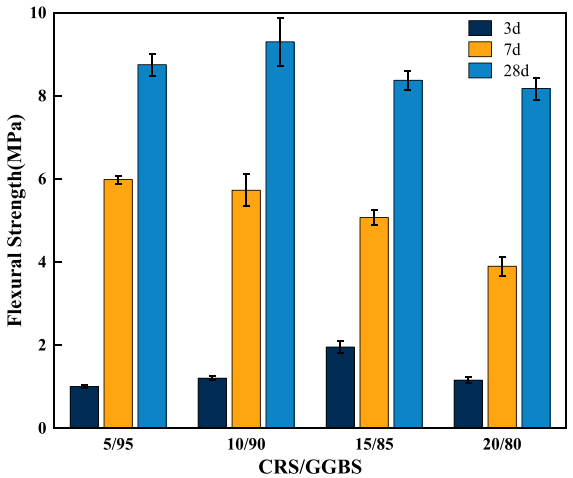

Fig. 9. Influence of CRS/GGBS ratio on the flexural strength at 3, 7 and 28 days.

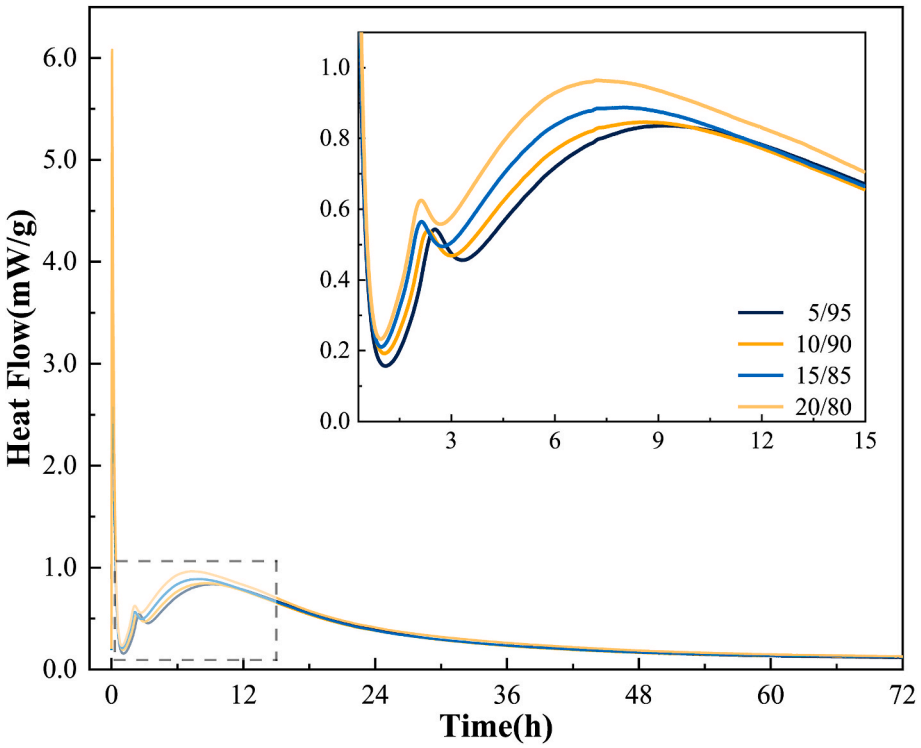

Fig. 10. Heat flow curve of blends with different CRS/GGBS ratios.

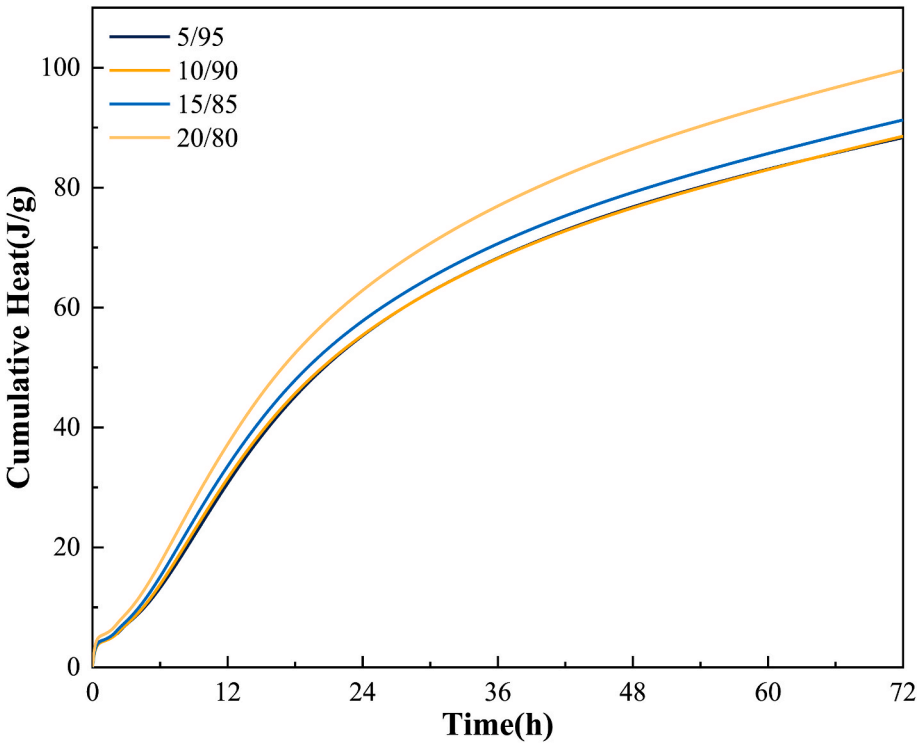

Fig. 11. Cumulative heat release curve of blends with different CRS/GGBS ratios.

control in concrete is an issue such as mass concrete.

3.1.3. Hydration products

The XRD patterns of CRS/GGBS samples at 28 days are depicted in Fig. 12 with identified phases. Calcium silicate hydrate (CSH, primarily identified at 2θ = 22.4° and 29.6°), hydrotalcite (HT, typically represented as $Mg_6Al_2CO_3(OH)_{16}{\cdot}4H_2O$, identified at 2θ = 11.5°) and calcium hydroxide (CH, identified at 2θ = 18.1°, 34.0° and 50.8°) are present in all mixtures. Hydrotalcite is a kind of Mg-Al-rich mineral with layered double hydroxide structure [41], and is advantageous in terms of mechanical properties and shrinkage reduction [42]. The presence of calcite (2θ = 48.5°) may result from the carbonation of calcium hydroxide during curing process. As the content of CRS increases, the diffraction peaks of CH are notably intensified. CASH in the form of katoite ($Ca_3Al_2(SiO_4)(OH)_8$) observed at the reflection of 2θ = 32.4°, which is attributed to the incorporation of aluminum released from GGBS into CSH [37]. As the CRS content increases from 5 % to 20 %, the intensity of CH peaks significantly increases [43]. The high CH content in CRS provides an alkaline environment for the system, but excessive addition (as in 20/80) results in an insufficient dissolution rate of GGBS to consume all CH, leaving residual CH in crystalline form. The weak interfacial bonding between this residual CH and the gel phase leads to reduced mechanical performance [44]. In 15/85, an optimal OH^- concentration promotes the synergistic dissolution of CaO, SiO_2, and Al_2O_3 in GGBS, forming C-A-S-H gel. Its three-dimensional network structure significantly enhances matrix compactness. HT promote the development of more uniform and dense C-A-S-H gel network by consuming aluminum ions, thereby synergistically optimizing the pore structure and permeability resistance of the matrix.

The results of TGA and derivative of thermogravimetry analysis (DTG) for CRS/GGBS samples at 28 days are presented in Fig. 13. The weight loss observed between 30 and 200 °C is mainly attributed to the decomposition of CSH and CASH [45,46], which are known to contribute significantly to the development of strength [46]. The broader peaks in DTG curves, ranging from 200 to 380 °C, are indicative of the decomposition of hydrotalcite and hydrotalcite-like phases [47]. The weight loss observed within the temperature range of 400–500 °C is attributed to the dehydration of calcium hydroxide. With the increase of CRS content in CRS/GGBS mixtures, more C-S-H, HT and calcium hydroxide are found. The mass loss within the 400–500 °C range directly correlates with CRS content, indicating incomplete consumption of excess CH by GGBS. This residual CH exhibits inadequate bonding with the gel phase, thereby contributing to the observed reduction in compressive strength. Additionally, minor mass loss detected from 600 to 900 °C results from natural carbonation due to ambient CO_2 exposure, consistent with XRD analytical results.

The FTIR results for the CRS/GGBS samples at 28 days are plotted in Fig. 14. The O-H band at 3644 cm^{-1} corresponds to the presence of Ca $(OH)_2$ [48]. The band at 3435 cm^{-1} and 1638 cm^{-1} can be attributed to hydroxyl bands through hydrogen bands and H-O-H bending vibrations in water, respectively [49,50]. The presence of these bands is due to crystalline H_2O in CSH [51]. Absorption peak of CO_3^{2-} at 1432 cm^{-1} indicates the presence of calcite and hydrotalcite [52]. The *Si*-O band at 972 cm^{-1} indicates the presence of

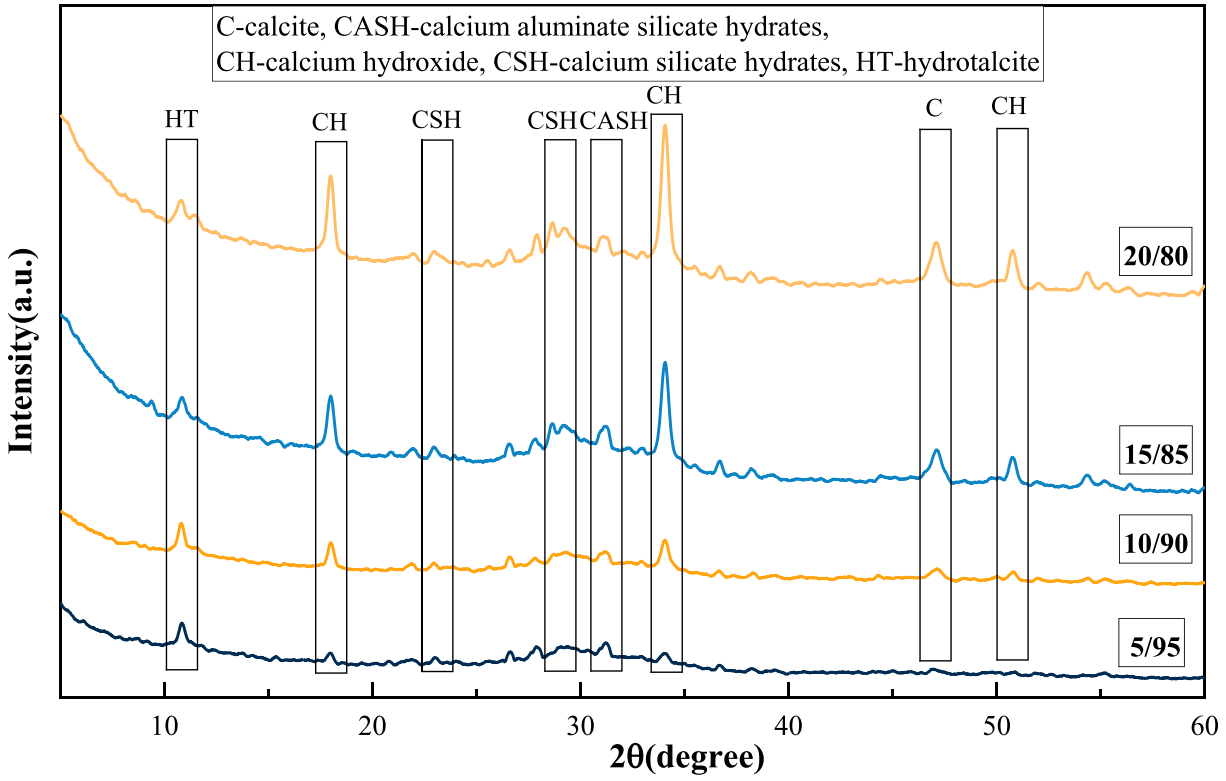

Fig. 12. XRD patterns of 28 days cured samples with different CRS/GGBS ratios.

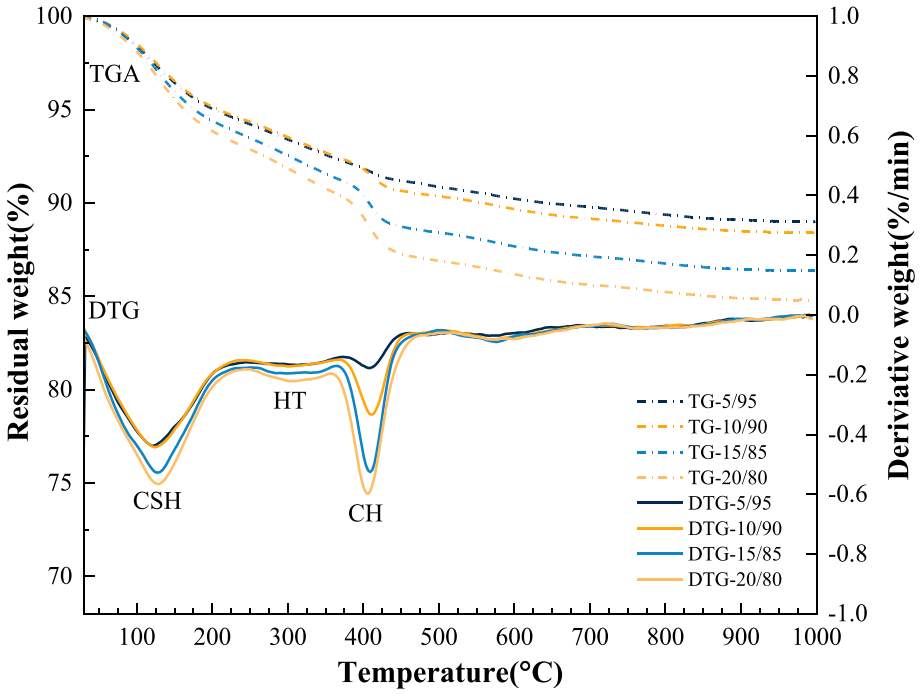

Fig. 13. TG-DTG curves of 28 days cured samples with different CRS/GGBS ratios.

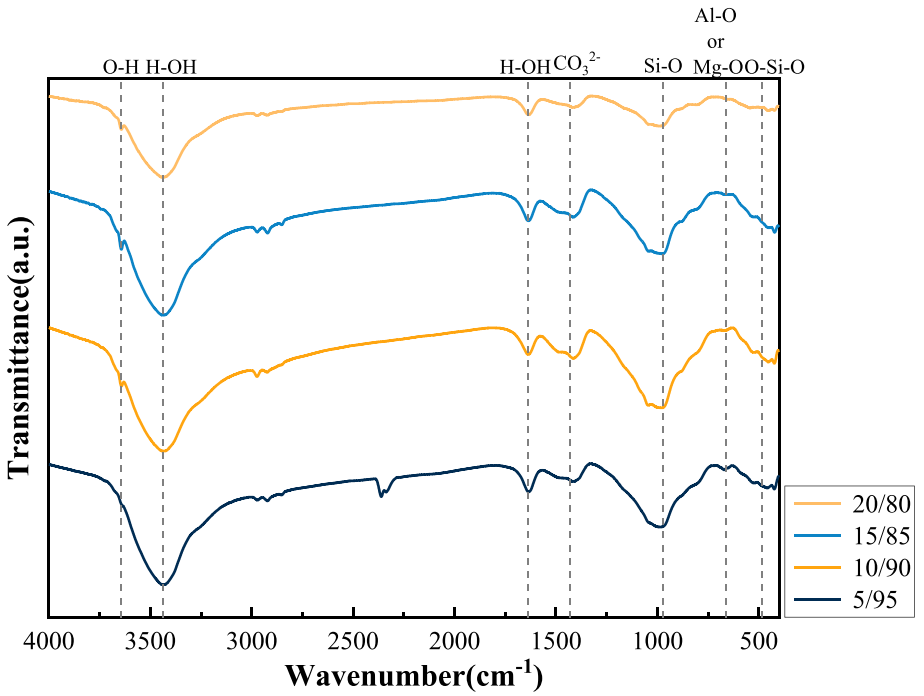

Fig. 14. FTIR curves of 28 days cured samples with different CRS/GGBS ratios.

CSH [53]. Al-O or Mg-O band around 663 cm^{-1} suggests the formation of hydrotalcite [54]. The broad component at 483 cm^{-1} can be assigned to O-Si-O bending modes of SiO_4 tetrahedra of the GGBS [55], indicating the presence of unreacted GGBS in the samples.

The XRD, TGA, and FTIR analysis results indicate that the calcium hydroxide in CRS promotes the hydration of GGBS, generating more hydration products, including CSH, CASH, and hydrotalcite phases. On the other hand, if too much CRS was added, the crystal calcium hydroxide concentration in the matrix would rise and the GGBS content which is the primary source of hydration products

would drop, resulting in a reduction in strength [37].

3.2. Foamed lightweight concrete

3.2.1. Fresh and mechanical properties

Table 8 shows the fresh properties of foamed lightweight concrete. The measured wet density aligns closely with the target density. For all mixtures, the measured flowability falls between 170 mm and 190 mm, satisfying the standards for in-place casting. The dry density is observed to decrease as the foam content increases.

The compressive strengths of foamed lightweight concrete at 3, 7, and 28 days are presented in Table 9. The compressive strength increases with curing time and densities as predicted. The strength grows much faster after 7 days. The ratio between the measured 7 and 28 days compressive strength are 0.175, 0.255, 0.242, 0.233 for WD600, WD700, WD800 and WD900, respectively, which is much higher than normal concrete and cement paste [56]. Furthermore, it is noted that although the standard mortar strength of CRS/GGBS is only about half of 42.5 OPC, the compressive strength of CRS/GGBS foamed lightweight concrete exceeds that of OPC foamed lightweight concrete. Compared with OPC foamed lightweight concrete [57], at a wet density of 700 kg/m^3, the 28 d compressive strength of CRS/GGBS foamed lightweight concrete is 20.98 % greater than that of OPC foamed lightweight concrete.

The elastic modulus is presented in Table 9. It gradually increases with wet density. Compared with OPC, CRS/GGBS foamed lightweight concrete shows a lower elastic modulus at the same density [58]. The ratio between compressive strength and modulus is around 2.13–2.24 $\times$ 10^{-3}. This indicates that the CRS/GGBS blends foamed lightweight concrete is more deformable at the peak stress state.

3.2.2. Rheology behavior

Figs. 15 and 16 illustrate the fitted results after applying the Bingham model for fresh paste blends and foamed lightweight concrete to the data collected between 180 and 240 s of shearing. For blends with no foam, as the water/binder ratio decreases, the plastic viscosity and yield stress increase. Specifically, Table 10 shows that the yield stress escalates from 1.430 Pa to 9.166 Pa, and the plastic viscosity increases from 0.107 Pa s to 0.184 Pa s with a reduction in the water/binder ratio from 0.7 to 0.6. The incorporation of foam leads to a marked increase in both plastic viscosity and yield stress (see in Table 10). This is attributed to the physical obstruction of bubble interfaces restricting particle mobility [59], and increased interparticle friction within the confined paste matrix. The dominant influence of foam content over water-to-binder ratio aligns with observations that entrained air significantly alters the paste's shear-thinning behavior and yield stress threshold [60]. The increase rate is defined as the ratio between the measured rheological parameters after and before adding the foam. The decreasing rate of yield stress increase with rising foam content suggests a critical volume fraction effect. Beyond this threshold, bubble coalescence and reduced inter-bubble spacing diminish the interfacial resistance per unit volume [61], while increased lubrication from surplus air may offset viscous effects [62].

3.2.3. Pore structures

Fig. 17 shows the average plane porosity of foamed lightweight concrete along height. It is shown that the variation coefficient of the plane porosity of each mixture is within 2 %, indicating that the spatial distribution of introduced air voids is relatively uniform. The average porosity of foamed lightweight concrete falls from 0.3354 to 0.2670 when the density increases from 600 kg/m^3 to 900 kg/m^3. This reported porosity value is significantly lower than the actual porosity, which also includes capillary and gel pores, because of the limitation of X-CT resolution.

Paste specimens with the same dimensions (100 mm $\times$ 100 mm $\times$ 100 mm) and without foam were cast, adopting the identical mix proportions as those listed in Table 3. Three parallel specimens were prepared for each mix proportion to ensure test reproducibility. After standard curing for 28 days, the specimens were dried to a constant weight, and their dry density was subsequently determined. Based on this dry density data, the introduced porosity (P) of the foamed lightweight concrete was calculated using the following formula.

$$P = 1 - \frac{\rho_{FLC}}{\rho_{Paste}}$$

where, ρ_{FLC} and ρ_{Paste} represent the dry densities of the foamed lightweight concrete specimen and the cement paste specimen, respectively. As noted earlier, due to the limitations of X-CT resolution, pores with diameters smaller than this resolution cannot be effectively identified. Thus, the porosity determined via X-CT is lower than the actual introduced porosity, and detailed data regarding this comparison are presented in Table 11.

A statistical analysis is performed on the foamed lightweight concrete pore size distribution, and the findings are displayed in

Table 8
Fresh properties of foamed lightweight concrete.

Wet density (kg/m^3)	Measured wet density (kg/m^3)	Flowability (mm)	Dry density (kg/m^3)
600	609 ± 15	167 ± 4	437 ± 8
700	691 ± 12	171 ± 5	514 ± 11
800	801 ± 11	189 ± 3	602 ± 7
900	890 ± 8	196 ± 3	680 ± 16

Table 9
Mechanical properties of foamed lightweight concrete.

Wet density (kg/m^3)	Compressive strength (MPa)			Elastic modulus (MPa)	Ratio between compressive strength and modulus
	3-day	7-day	28-day		
600	0.142	0.484	2.763	1250.1	2.210×10^{-3}
700	0.216	0.884	3.460	1547.3	2.236×10^{-3}
800	0.288	1.056	4.356	2034.5	2.141×10^{-3}
900	0.355	1.302	5.586	2610.6	2.139×10^{-3}

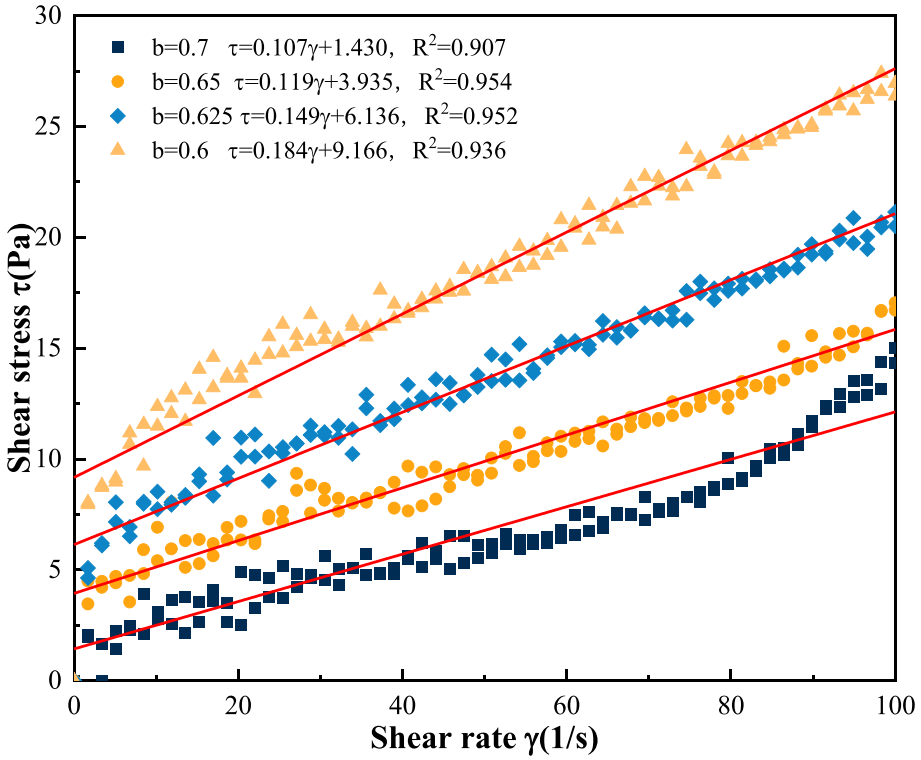

Fig. 15. Shear stress-shear rate curve of blended pastes along time.

Fig. 18. Similar pore size distributions are found for all mixtures. It can be seen that most of the pores fall in the range of 50–100 μm. Compared with OPC foamed lightweight concrete whose pore size is concentrated between 200 μm and 800 μm [58], the CRS/GGBS foamed lightweight concrete has a much finer pore structure. A smaller and more uniform pore size distribution is conducive to enhance the strength of foamed lightweight concrete at equivalent densities [63]. This partly explains why CRS/GGBS foamed lightweight concrete at the same density has higher strength compared to the OPC counterpart.

The performance of foamed lightweight concrete is somewhat influenced by the shape of pores. Herein, we adopt a shape factor to describe pore morphology. The shape factor is made up of the flatness index and the elongation index. These indices are determined using ImageJ software by correlating the lengths of the pore axes in three orthogonal directions to the axes of an ellipsoid. The three axes are perpendicular to one another, though they do not necessarily intersect at a single point [64]. The elongation index is traditionally quantified by the ratio l/L, where L denotes the longest dimension and l is the dimension that is the longest and perpendicular to L, whereas the true flatness index is more accurately represented by the ratio S/l, with S being the smaller dimension that is perpendicular to both L and l.

A typical Zingg diagram of the foamed lightweight concrete is seen in Fig. 19. Four areas are identified based on the dividing line of 0.67: discoid, spheroid, blade, and rod. These regions correspond to the flatness and length of pores. Table 12 displays the precise division rules [65]. It can be seen that most of the pores are in the shape of spheroid and rod. Fig. 20 illustrates the frequency distribution of pore shapes in foamed lightweight concrete across various densities. It can be seen from the figure that the pore shape distribution of foamed lightweight concrete with different wet densities is similar, and about 55 % of the pores are spheroid, 35 % of the pores are rod shaped. More than half of the voids are approximately spheroid, and they have lower stress concentrations around compared to sharp elongated pores. The CRS/GGBS foamed lightweight concrete has much more spherical pores than cement foamed lightweight concrete as reported by Guo et al. [66]. This results in higher strength of CRS/GGBS foamed lightweight concrete.

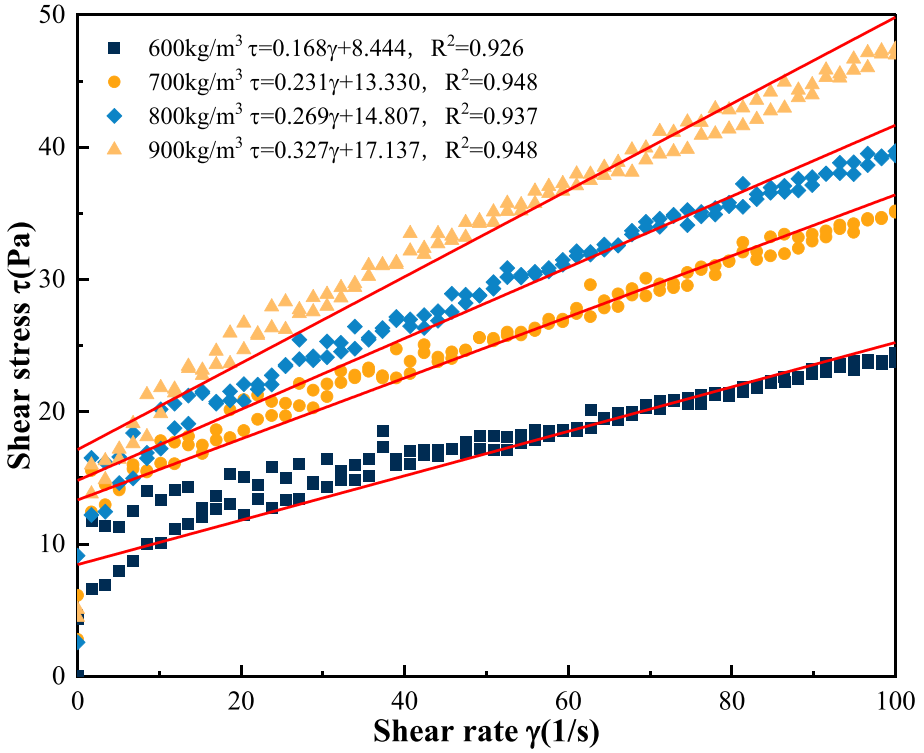

Fig. 16. Shear stress-shear rate curve of foamed lightweight concrete.

Table 10
The yield stress and plastic viscosity of blended pastes and foamed concrete.

Wet density (kg/m^3)	W/b ratio	Foam content (%)	Yield stress (Pa)			Plastic viscosity (Pa·s)		
			Blend	Foamed concrete	Increase degree (%)	Blend	Foamed concrete	Increase degree (%)
600	0.7	7.62	1.430	8.444	490.49	0.107	0.168	57.01
700	0.65	5.73	3.935	13.330	238.75	0.119	0.231	94.12
800	0.625	4.42	6.136	14.807	141.31	0.149	0.269	80.54
900	0.6	3.44	9.166	17.137	86.96	0.184	0.327	77.72

The pore sphericity distribution of foamed lightweight concrete is depicted in Fig. 21. It is evident that the sphericity of foamed lightweight concrete with different wet densities is concentrated at 0.8–1.0, accounting for about 65 % in total. By comparing the pore size distribution, it is found that the proportion of voids with sphericity of 0.9–1.0 is approximately the same as that of the voids with a size of 50–70 μm, that is, the smaller voids have higher sphericity. This is in accordance with the observation reported by Yang et al. [67]. This can be attributed to the fact that large voids in general form due to bubble ripening and coalescence making them irregular.

The mechanical performance of the porous materials is significantly influenced by the pore size and spatial distribution of the pores, as can be discerned from the segmented pore phase within ROI. Pore spacing, defined as the minimum distance between pores [58], is depicted in Fig. 22, which shows the distribution of pore spacing in foamed lightweight concrete. It can be seen from the figure that the distribution range of pore spacing is 0–150 μm, about 75 % of it is concentrated within 0–15 μm, while the spacing within 50–150 μm is less than 2 %, which reflects the uniformity and compactness of pore distribution of the prepared foamed lightweight concrete.

The pore structure of foamed lightweight concrete exerts a direct and pronounced influence on its mechanical properties. To quantitatively assess how various pore structure parameters affect compressive strength, this study leverages the theory of grey relational analysis (GRA) to calculate the grey relational grade between multiple pore characteristic parameters of foamed lightweight concrete and its compressive strength, thereby quantifying the correlation between these parameters and compressive strength. GRA assesses the correlation degree between different factors by analyzing the similarities or dissimilarities in their developmental patterns [67]. A key advantage of this method is that it eliminates the need to consider the specific distribution of data; even when data availability is limited or data sets are incomplete, it can still unveil the intrinsic relationships between factors by computing their relational degrees. The essence of GRA resides in identifying whether various factors exert an influence on a specific target variable. Through systematic quantitative calculations, GRA compares the grey relational degrees between individual sequences (representing

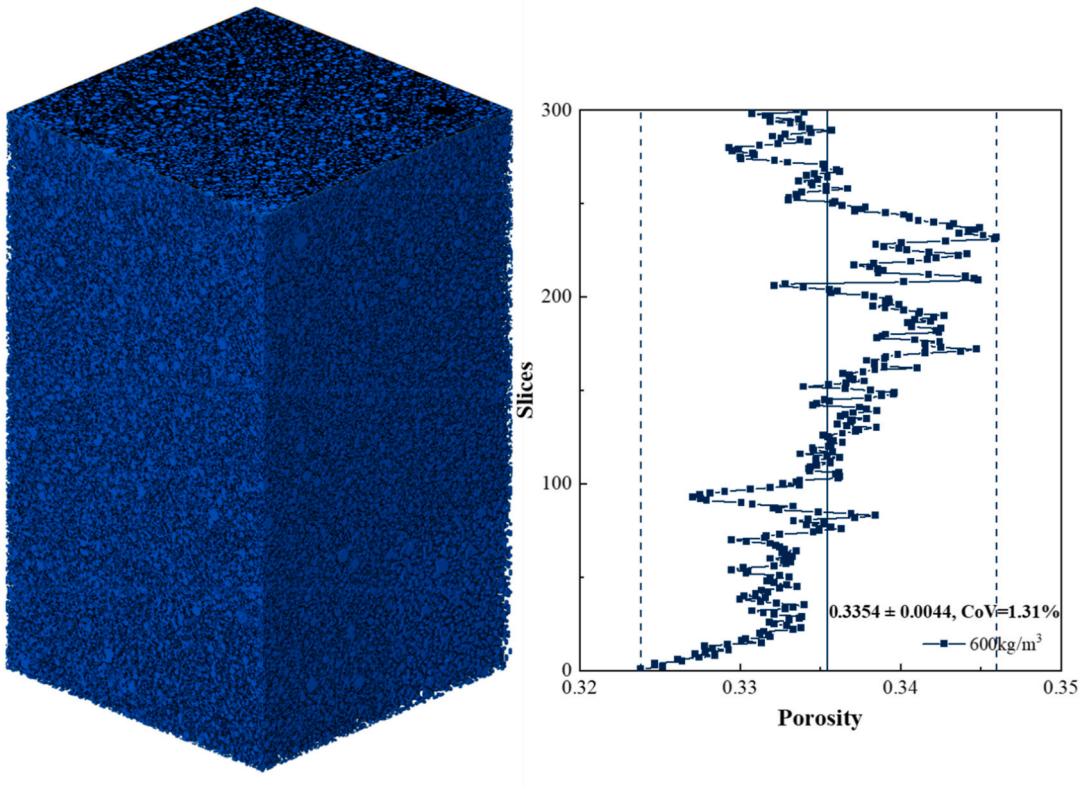

(a)

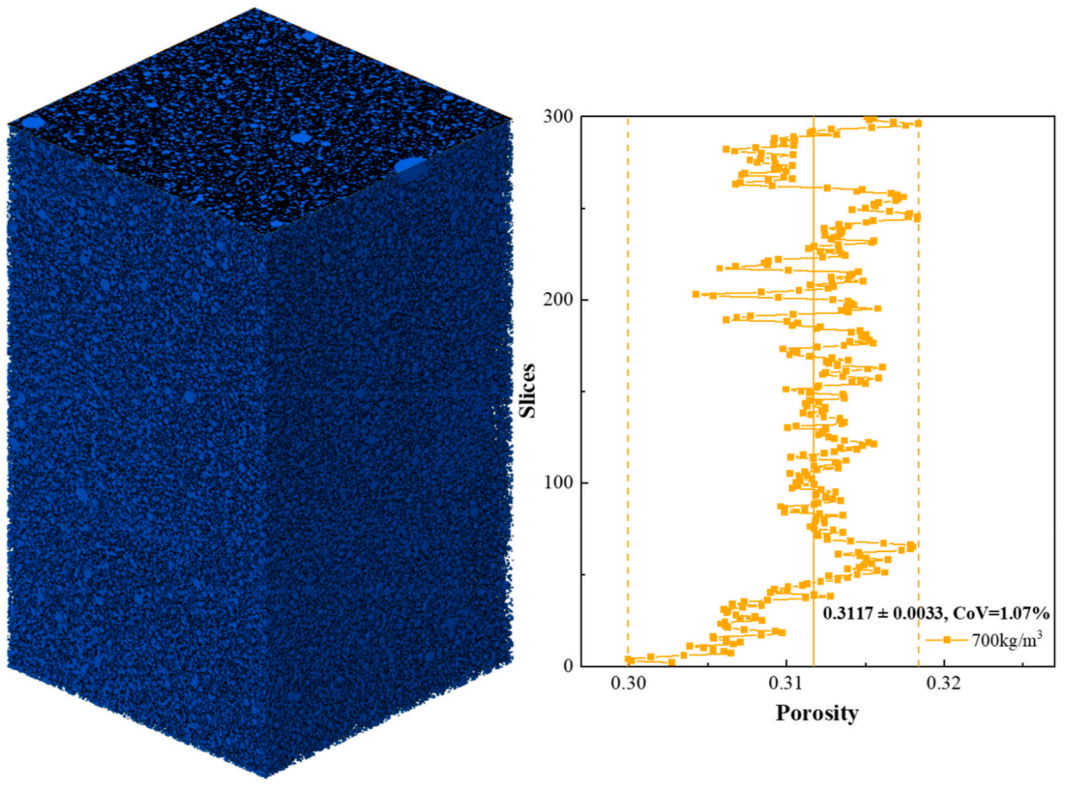

(b)

Fig. 17. Porosity of foamed lightweight concrete at different height. (a) 600 kg/m^3, (b) 700 kg/m^3, (c) 800 kg/m^3, (d) 900 kg/m^3.

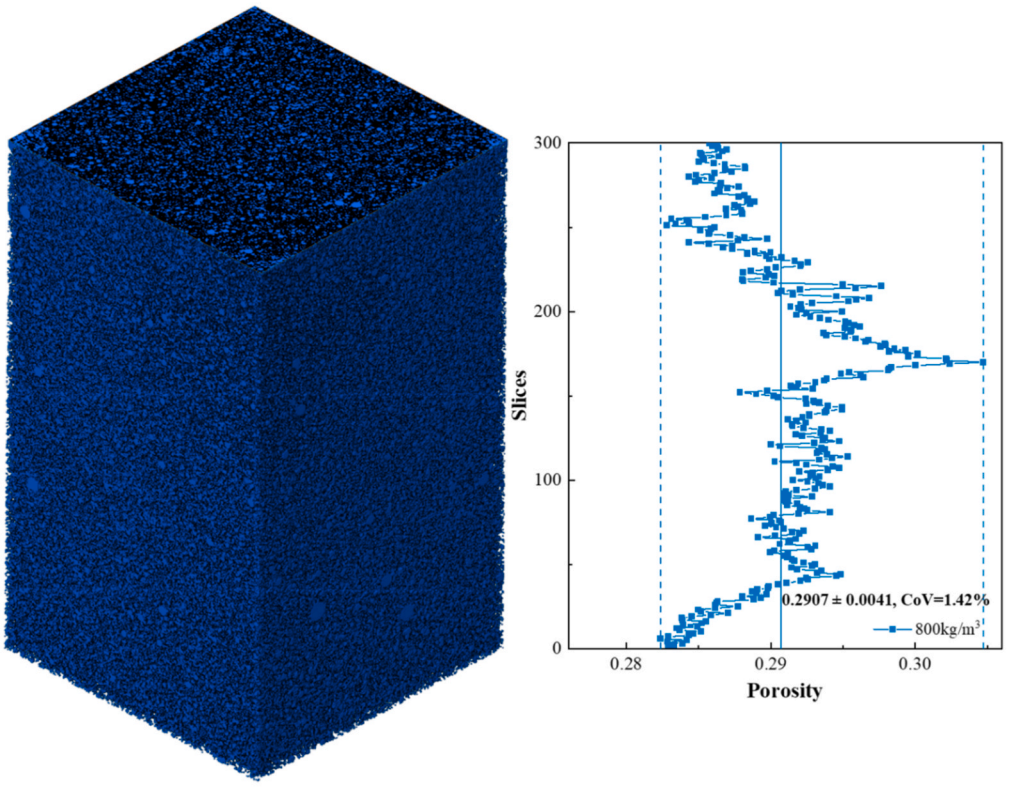

(c)

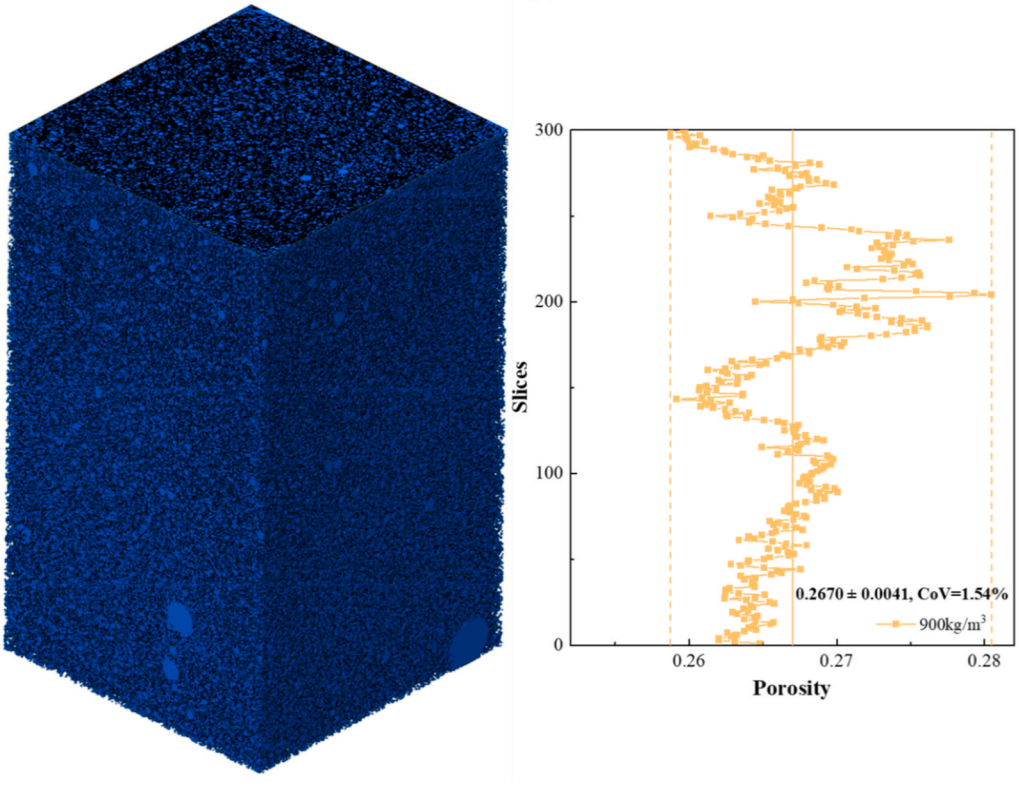

(d)

Fig. 17. (*continued*).

Table 11
The X-CT porosity and the introduced porosity of foamed lightweight concrete.

Wet density (kg/m^3)	The X-CT porosity (%)	The introduced porosity (%)
600	33.54	51.67
700	31.17	50.03
800	29.07	48.56
900	26.70	46.27

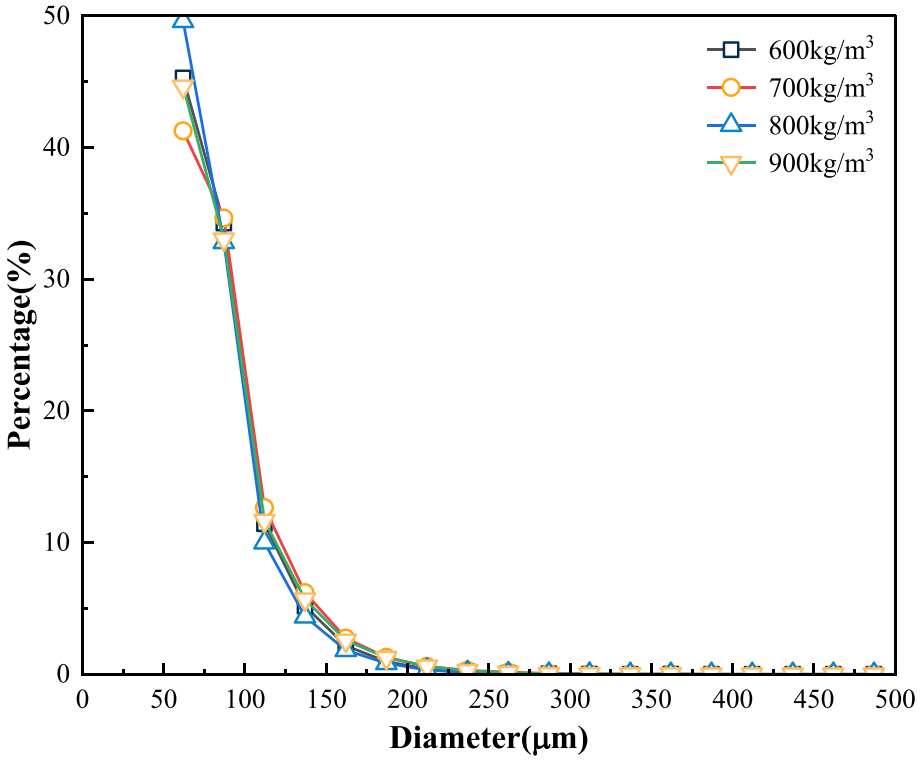

Fig. 18. Pore size distribution of foamed lightweight concrete.

different factors) and a reference sequence (representing the target variable), ultimately determining the extent of each factor's impact on the target variable [68].

The compressive strength of foamed lightweight concrete is set as the reference sequence Y, and the pore structure parameters as the comparison sequence X, where $Y = \{y_i | i = 0, 1, 2, \cdots\}$, $X = \{x_i | i = 0, 1, 2, \cdots\}$, $y_i(k) \in Y$, $x_i(k) \in X$, $k = 1, 2, \cdots$. The steps for calculating the grey relational grade are as follows.

$$x_i(t) = \frac{x_i(k) - x_{i\,\min}}{x_{i\,\max} - x_{i\,\min}} \Big/ y_i(t) = \frac{y_i(k) - y_{i\,\min}}{y_{i\,\max} - y_{i\,\min}}$$

$x_{i\,\min}/y_{i\,\min}$, $x_{i\,\max}/y_{i\,\max}$ represent the minimum and maximum values of x_i/y_i respectively; $x_i(k)$ is the parameter value; $y_i(k)$ is the strength value.

$$\Delta x_i(t) = |y_i(t) - x_i(t)|$$

$$\xi(x_i(k), y_i(k)) = \frac{\min\min \Delta x_i(t) + \zeta \max\max \Delta x_i(t)}{\Delta x_i(t) + \zeta \max\max \Delta x_i(t)}$$

ζ is generally taken as 0.5; $\xi(x_i(k), y_i(k))$ is the grey relational coefficient between the strength and the pore structure parameter.

$$r(x_i(k), y_i(k)) = \frac{1}{n} \sum_{k=1}^{n} \xi(x_i(k), y_i(k))$$

Table 13, Tables 14, and Table 15 present the calculated grey relational grades between pore structure parameters (i.e., pore size, pore sphericity, and other pore characteristics) and the compressive strength of foamed lightweight concrete. The results indicate that

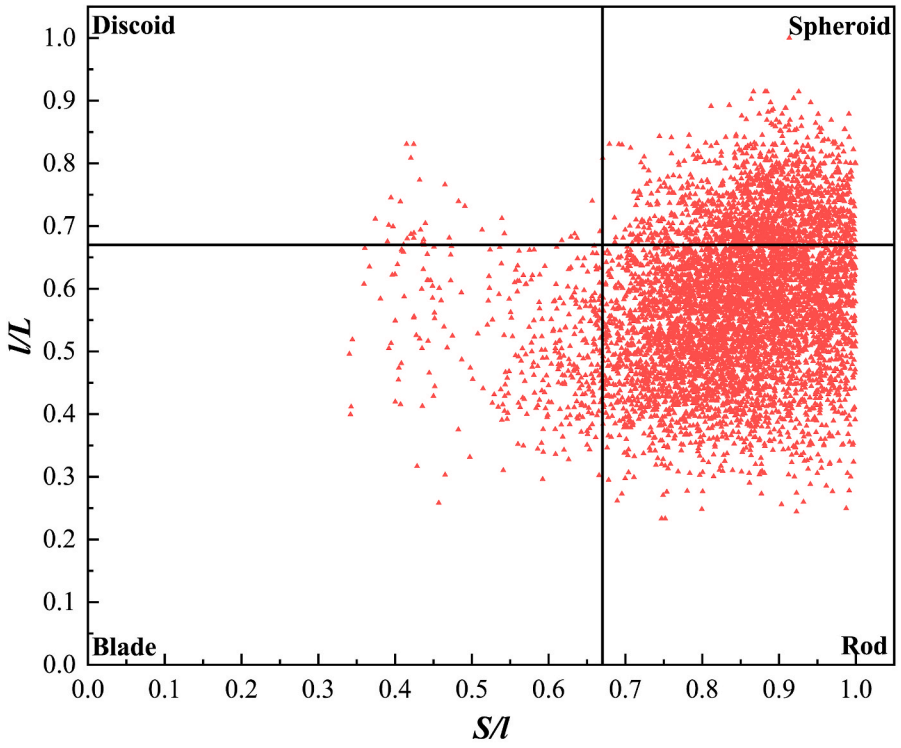

(a)

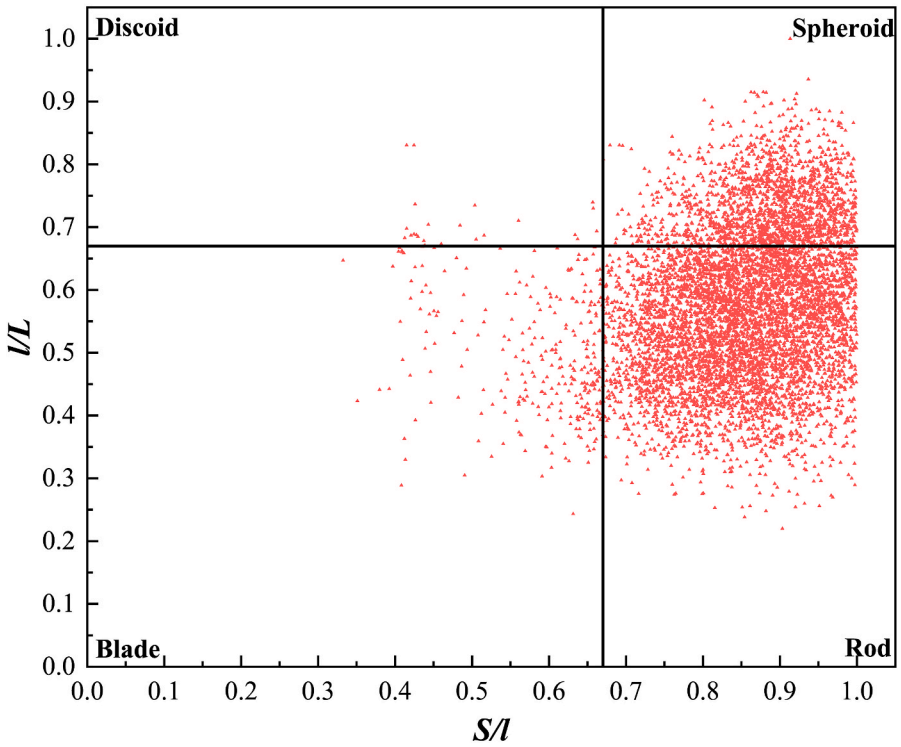

(b)

Fig. 19. Zingg diagram of foamed lightweight concrete. (a) 600 kg/m^3, (b) 700 kg/m^3, (c) 800 kg/m^3, (d) 900 kg/m^3.

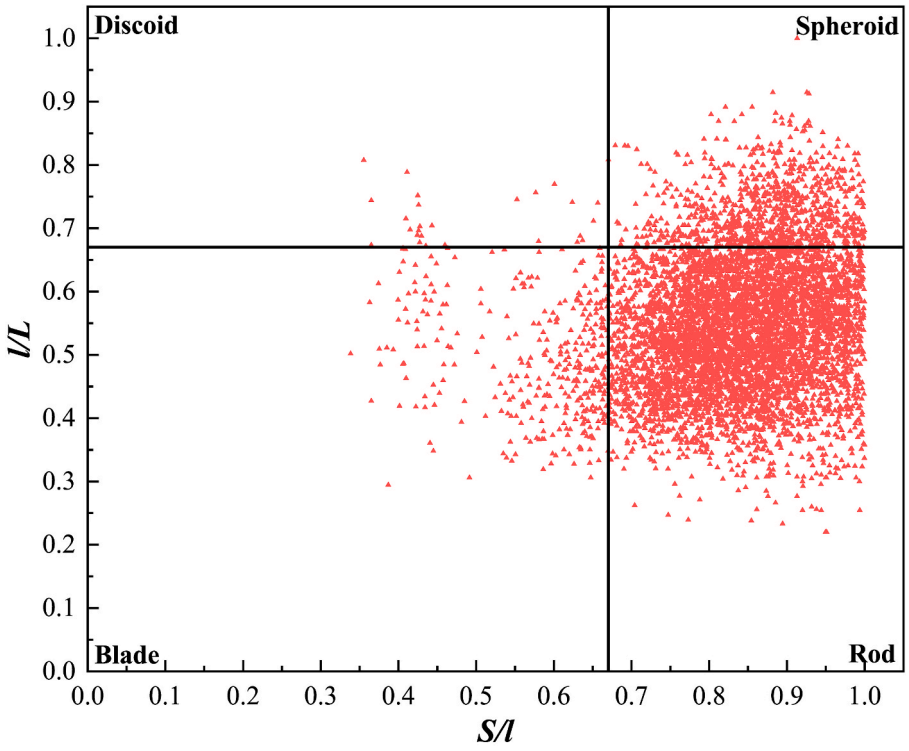

(c)

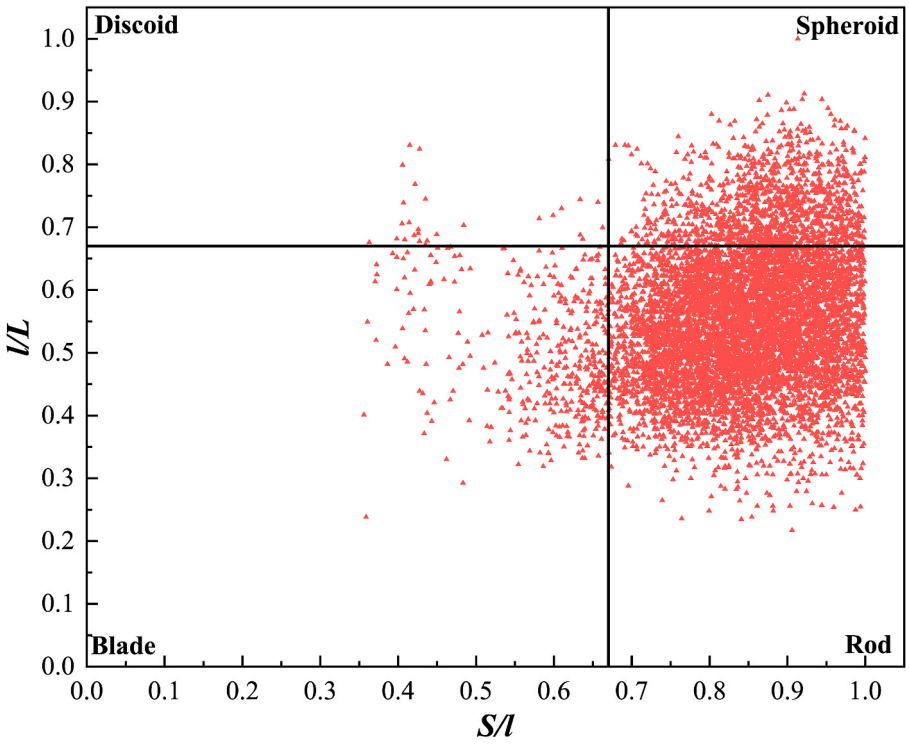

(d)

Fig. 19. (*continued*).

Table 12
Pore shape classification based on shape factor.

Class	Elongation index (l/L)	Flatness index (S/l)	Shape
1	>0.67	<0.67	Discoid
2	>0.67	>0.67	Spheroid
3	<0.67	<0.67	Blade
4	<0.67	>0.67	Rod

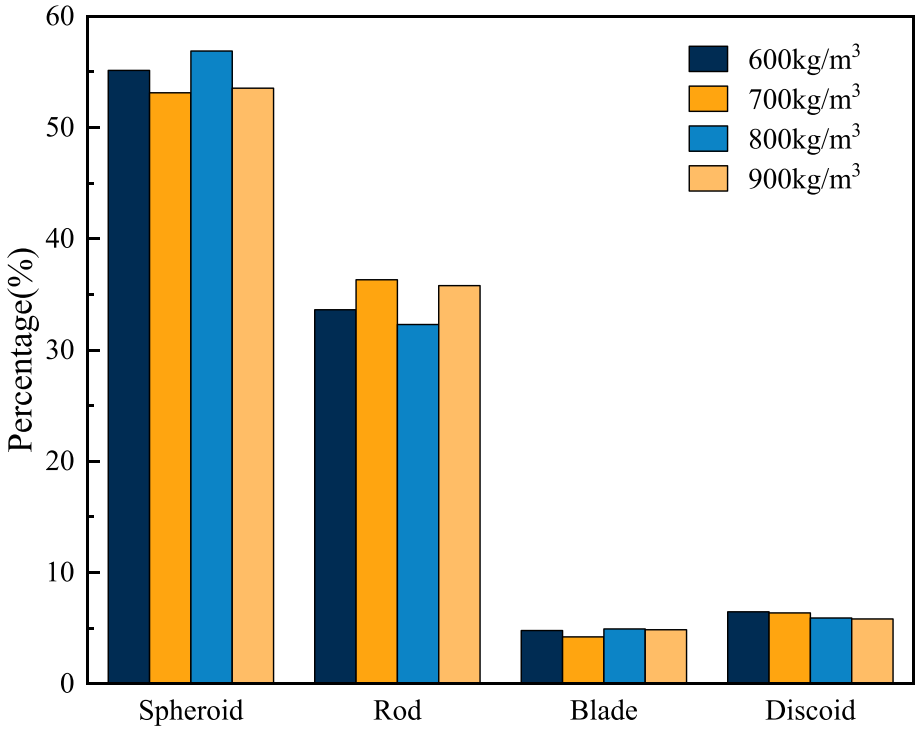

Fig. 20. Shape factor distribution of foamed lightweight concrete.

pores within the size range of 50–100 μm exhibited the highest relational grade with the compressive strength of FLC, reaching 0.7225. This finding suggests that increasing the proportion of small-sized pores constitutes the primary factor governing the material's compressive strength. Among the different pore sphericity intervals, the interval corresponding to a sphericity of 0.9–1.0 (i.e., the highest sphericity category) showed the strongest relational degree with compressive strength, reaching 0.6639. This implies that pores with high sphericity exert the most significant influence on the strength of FLC, which can be attributed to the fact that pores with a shape closer to spherical facilitate more uniform stress distribution within the material, thereby enhancing compressive strength.

Additionally, spheroid and discoid pores, specifically those with the elongation index (l/L) exceeding 0.67, exhibited the highest relational grade with the compressive strength of FLC, further confirming their dominant role in regulating strength. Notably, with an increase in wet density, the compressive strength of FLC increases, whereas its porosity decreases. In the grey relational grade calculation, the focus is on quantifying the similarity of change trends between variables, rather than distinguishing between positive and negative correlations. It is important to note that the decrease in porosity and the increase in compressive strength exhibit a negative correlation. In grey relational analysis, however, calculations are performed using absolute differences. Specifically, following data normalization, trends that are asynchronous are classified as non-synchronous, which justifies the observed low relational degree between porosity and compressive strength. In conclusion, foamed lightweight concrete exhibits higher compressive strength when its pores have a shape closer to spherical and the material possesses higher compactness.

3.3. Global warming potential

Table 16 displays the global warming potential (GWP) for 1 m^3 foamed lightweight concrete for raw materials, transportation, and production, in that order. In the whole life cycle, the GWP of CRS/GGBS foamed lightweight concrete is about 56.5–90.1 kg/m^3, while the CO_2 equivalent of OPC foamed lightweight concrete is 308.5–469.2 kg/m^3. The GWP of CRS/GGBS foamed lightweight concrete in the whole life cycle is significantly lower than that of OPC foamed lightweight concrete, about one fifth of it. The preparation stage for

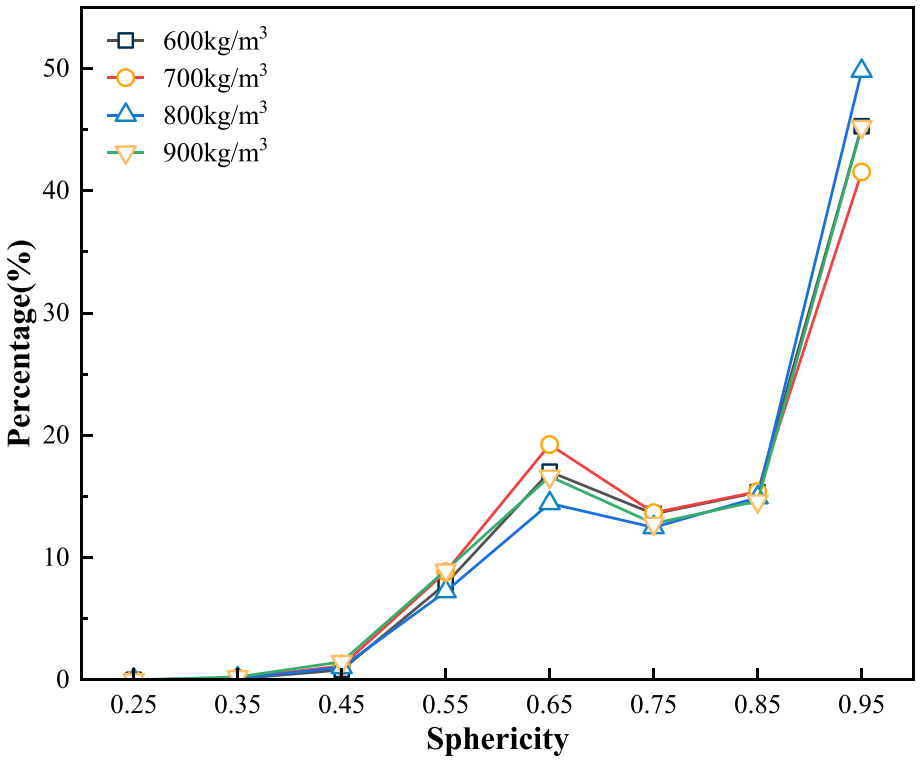

Fig. 21. Sphericity distribution of foamed lightweight concrete.

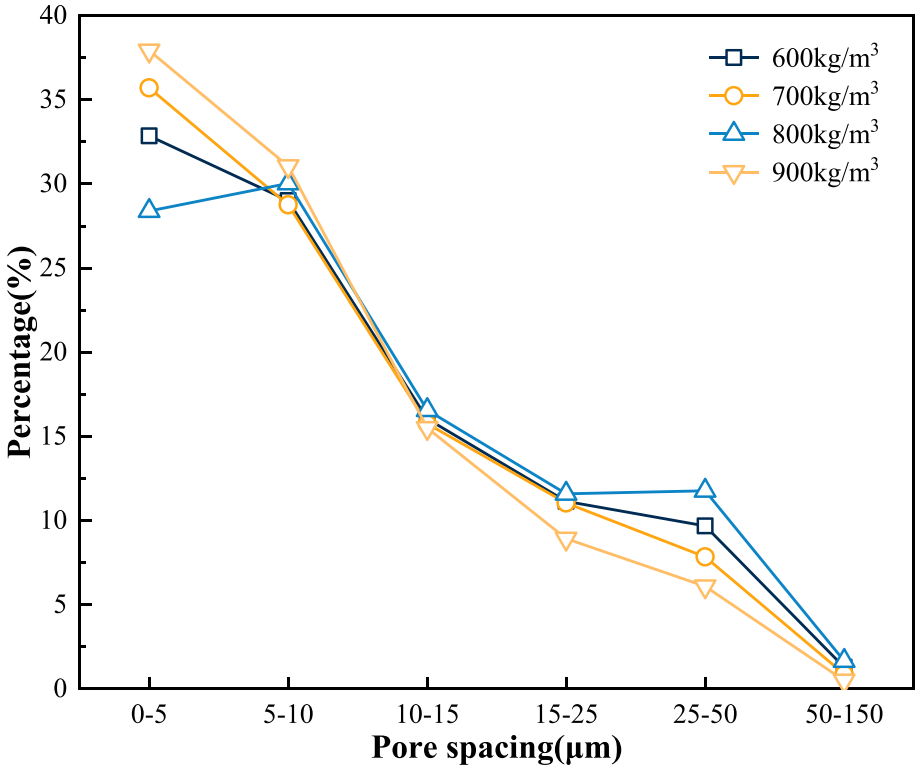

Fig. 22. Pore spacing distribution of foamed lightweight concrete.

Table 13
Grey correlation between pore size and compressive strength of foamed lightweight concrete.

Pore size (μm)	50–100	100–150	150–200	200–250	>250
Compressive strength	0.7225	0.5951	0.6000	0.6299	0.6062

Table 14
Grey correlation between sphericity and compressive strength of foamed lightweight concrete.

Sphericity	0–0.6	0.6–0.7	0.7–0.8	0.8–0.9	0.9–1.0
Compressive strength	0.5196	0.44225	0.5016	0.5349	0.6639

the raw materials is the main cause of the decrease. According to Fig. 23, the production of OPC accounts for about 91 % of CO_2 emission in 1 m^3 OPC foamed lightweight concrete, whereas CRS/GGBS foamed lightweight concrete accounts for 47 % of the missions. For CRS/GGBS foamed lightweight concrete, transportation accounts the most carbon emission. When the construction site is close to the plants with solid wastes, the carbon reduction advantage of CRS/GGBS foamed lightweight concrete become more obvious.

Typically, cement transportation distances range from 50 to 350 km. Based on relevant literature [31], the distance for cement in this study was set at 161 km. Transportation distances for CRS and GGBS from 70 to 500 km; following literature review and consideration of actual conditions, 200 km was selected in this study [36]. Under the worst-case scenario, transportation distances were set to 50 km for OPC and 500 km for CRS and GGBS. The LCA results for foamed lightweight concrete (FLC) at different stages, derived from calculations, are detailed in Table 17. Crucially, even under the worst-case scenario, FLC with equivalent wet density using the CRS/GGBS system exhibited a global warming potential (GWP) approximately 35 % that of OPC formulations. This significant reduction underscores the substantial potential of CRS/GGBS to replace cement in FLC production for mitigating carbon emissions.

Furthermore, analysis revealed that transportation-related carbon emissions contributed only about 3 % to the total GWP in the cement system under this worst-case scenario. In contrast, transportation emissions accounted for a dominant 70 % of the total GWP in the CRS/GGBS system. This highlights the non-negligible impact of transportation distance on LCA outcomes. In conclusion, despite the significant sensitivity of the CRS/GGBS system to transportation distance, replacing OPC with CRS/GGBS in FLC production yielded a 65 % reduction in GWP even in the most unfavorable scenario. This demonstrates the considerable potential of this substitution strategy for carbon emission reduction within the civil engineering.

The substitution of OPC foamed lightweight concrete by CRS/GGBS to obtain comparable strength would lead to the reduction of a large amount of CO_2 emissions. In-depth development of the potential and sustainability benefits of applying CRS/GGBS foamed lightweight concrete in large infrastructure projects will mitigate the greenhouse gas emissions associated with cement production and enhance the resource recovery of industrial solid waste.

4. Conclusions

This study demonstrates the application of a novel CRS/GGBS binder system for producing sustainable foamed lightweight concrete, revealing the following key findings.

(1) An optimal CRS/GGBS ratio (10/90) is obtained for achieving the maximum compressive strength in the binder system. While the 28-day compressive strength of this blend is significantly lower than OPC, it exhibits superior flexural strength, indicating enhanced toughness and crack resistance.

Table 15
Grey correlation between pore structure parameters and compressive strength of foamed lightweight concrete.

Pore structure parameters	Porosity	Spheroid	Discoid	Rod	Blade
Compressive strength	0.5460	0.6565	0.7221	0.5755	0.5616

Table 16
LCA of foamed lightweight concrete at different stages.

Materials	Raw materials (CO_2 eq kg)	Transportation (CO_2 eq kg)	Foamed concrete production (CO_2 eq kg)	Total (CO_2 eq kg)
OPC-600	280.6	25.6	2.3	308.5
OPC-700	329.9	30.1	2.3	362.3
OPC-800	378.5	34.5	2.3	415.3
OPC-900	427.9	39.0	2.3	469.2
CRS/GGBS-600	26.3	27.9	2.3	56.5
CRS/GGBS-700	31.8	33.8	2.3	67.9
CRS/GGBS-800	37.0	39.4	2.3	78.7
CRS/GGBS-900	42.5	45.3	2.3	90.1

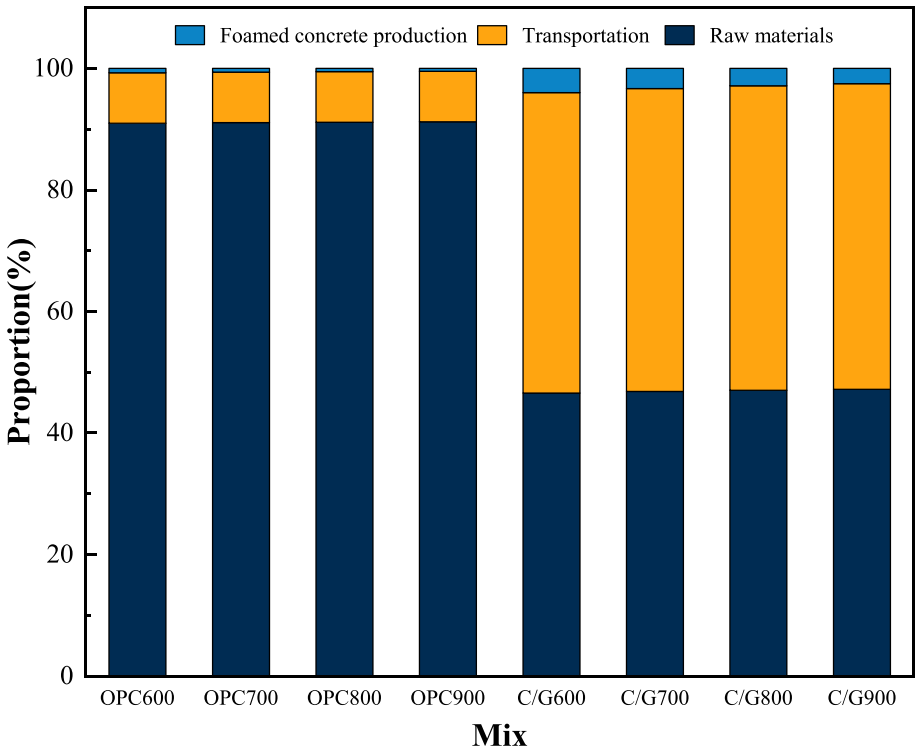

Fig. 23. GWP of foamed lightweight concrete at different stages.

Table 17
Under the worst-case scenario, LCA of FLC at different stages.

Materials	Raw materials (CO_2 eq kg)	Transportation (CO_2 eq kg)	Foamed concrete production (CO_2 eq kg)	Total (CO_2 eq kg)
OPC-600	280.6	8.06	2.3	290.96
OPC-700	329.9	9.44	2.3	341.64
OPC-800	378.5	10.8	2.3	391.6
OPC-900	427.9	12.18	2.3	442.38
CRS/GGBS-600	26.3	69.43	2.3	98.03
CRS/GGBS-700	31.8	84.21	2.3	118.31
CRS/GGBS-800	37.0	98.39	2.3	137.69
CRS/GGBS-900	42.5	113.01	2.3	157.81

(2) The CRS/GGBS binder exhibits remarkably low heat of hydration compared to OPC, primarily attributed to its distinct hydration products dominated by calcium silicate hydrate (CSH), calcium aluminate silicate hydrate (CASH), and hydrotalcite phases. This low hydration heat enables safer large-volume placements and effectively mitigating the risk of early-age thermal cracking.

(3) Foam content is the predominant factor governing the rheological properties specifically yield stress and plastic viscosity and flowability of CRS/GGBS foamed lightweight concrete, exerting a greater influence than water-binder ratio. The rate of increase in yield stress progressively diminishes as foam content rises, offering crucial insights into mixture design for achieving target workability.

(4) CRS/GGBS foamed lightweight concrete develops a significantly refined pore structure compared to conventional OPC foamed lightweight concrete. The majority of pores in CRS/GGBS foamed lightweight concrete fall within a finer range (50–100 μm), with notably smaller pore spacing (concentrated within 0–15 μm), exhibiting more spherical pore morphology and a denser spatial distribution. Grey relational analysis reveals that pores within 50–100 μm and sphericity >0.9 exhibit the highest correlation grades (0.7225 and 0.6639, respectively). This optimized pore structure is the primary factor responsible for delivering higher compressive strength in CRS/GGBS foamed lightweight concrete.

(5) CRS/GGBS foamed lightweight concrete achieves an approximately 80 % reduction in global warming potential over its entire life cycle compared to OPC foamed lightweight concrete. Moreover, while raw materials dominate carbon emissions >90 % in OPC foamed lightweight concrete, their contribution drastically decreases to around 47 % in CRS/GGBS foamed lightweight concrete, shifting the main emission source to transportation. This dramatic shift underscores the substantial inherent decarbonization potential of employing the CRS/GGBS binder system.

In conclusion, this research establishes the CRS/GGBS binder system as a low-carbon alternative for producing foamed lightweight concrete, offering a unique combination of enhanced flexural strength, reduced thermal cracking risk, superior pore structure leading to higher compressive strength, and a remarkable lifetime carbon footprint reduction.

CRediT authorship contribution statement

Zhi Ge: Writing – review & editing, Writing – original draft, Methodology, Funding acquisition. **Tianming Gao:** Writing – review & editing, Writing – original draft, Visualization, Methodology. **Hongzhi Zhang:** Writing – review & editing, Writing – original draft, Methodology, Funding acquisition. **Faliang Gao:** Writing – review & editing, Writing – original draft. **Qingyuan Yang:** Writing – original draft, Resources. **Xiaoyu He:** Writing – original draft, Resources. **Branko Šavija:** Writing – review & editing, Writing – original draft, Visualization, Methodology.

Declaration of competing interest

The authors declare no conflict of no interest.

Acknowledgements

This work was supported by National Natural Science Foundation of China (52378250), 111 Project (No. B21012), Natural Science Foundation of Shandong Province (No. ZR2024ME113) and “Unveiling and Commanding” Project of Jinan Municipal Bureau of Science and Technology (202323007).

Data availability

Data will be made available on request.

References

[1] W. She, Y. Du, G. Zhao, P. Feng, Y. Zhang, X. Cao, Influence of coarse fly ash on the performance of foam concrete and its application in high-speed railway roadbeds, Constr. Build. Mater. 170 (2018) 153–166.
[2] C. Zhang, Z. Zhu, Y. Zhang, F. Liu, Y. Yang, Y. Wan, W. Huo, L. Yang, Engineering properties and optimal design of foam lightweight soil composite fly ash: an eco-friendly subgrade material, J. Clean. Prod. 429 (2023) 139631.
[3] Y. Song, C. Xue, W. Guo, Y. Bai, Y. Shi, Q. Zhao, Foamed geopolymer insulation materials: research progress on insulation performance and durability, J. Clean. Prod. 444 (2024) 140991.
[4] K.-H. Yang, K.-H. Lee, J.-K. Song, M.-H. Gong, Properties and sustainability of alkali-activated slag foamed concrete, J. Clean. Prod. 68 (2014) 226–233.
[5] R.D. Hooton, J.A. Bickley, Design for durability: the key to improving concrete sustainability, Constr. Build. Mater. 67 (2014) 422–430.
[6] W. Sha, G.B. Pereira, Differential scanning calorimetry study of hydrated ground granulated blast-furnace slag, Cement Concr. Res. 31 (2) (2001) 327–329.
[7] R. Siddique, R. Bennacer, Use of iron and steel industry by-product (GGBS) in cement paste and mortar, Resour. Conserv. Recycl. 69 (2012) 29–34.
[8] C. Zhang, B. Li, Z. Chen, G. Wang, Research on the influence of microwave filler on the performance of recycled asphalt mixture, IOP Conf. Ser. Mater. Sci. Eng. 768 (2) (2020) 022006.
[9] Y. Kim, A. Hanif, M. Usman, M.J. Munir, S.M.S. Kazmi, S. Kim, Slag waste incorporation in high early strength concrete as cement replacement: environmental impact and influence on hydration & durability attributes, J. Clean. Prod. 172 (2018) 3056–3065.
[10] Y. Yi, M. Liska, A. Al-Tabbaa, Properties and microstructure of GGBS–Magnesia pastes, Adv. Cement Res. 26 (2) (2014) 114–122.
[11] S. Al-Otaibi, Durability of concrete incorporating GGBS activated by water-glass, Constr. Build. Mater. 22 (10) (2008) 2059–2067.
[12] F. Jin, K. Gu, A. Al-Tabbaa, Strength and hydration properties of reactive MgO-activated ground granulated blastfurnace slag paste, Cement Concr. Compos. 57 (2015) 8–16.
[13] S. Song, D. Sohn, H.M. Jennings, T.O. Mason, Hydration of alkali-activated ground granulated blast furnace slag, J. Mater. Sci. 35 (1) (2000) 249–257.
[14] M. Ben Haha, G. Le Saout, F. Winnefeld, B. Lothenbach, Influence of activator type on hydration kinetics, hydrate assemblage and microstructural development of alkali activated blast-furnace slags, Cement Concr. Res. 41 (3) (2011) 301–310.
[15] A.M. Rashad, Y. Bai, P.A.M. Basheer, N.B. Milestone, N.C. Collier, Hydration and properties of sodium sulfate activated slag, Cement Concr. Compos. 37 (2013) 20–29.
[16] S. Dwibedy, S.K. Parhi, S. Panda, S.K. Panigrahi, Performance of precursor characteristics in the realisation of geopolymer concrete: a review, Mag. Concr. Res. 76 (24) (2024) 1404–1423.
[17] K.-H. Yang, A.-R. Cho, J.-K. Song, S.-H. Nam, Hydration products and strength development of calcium hydroxide-based alkali-activated slag mortars, Constr. Build. Mater. 29 (2012) 410–419.
[18] Y. Liu, H. Wang, S. Tighe, D. Pickel, Z. You, Study on impact of variables to pavement preheating operation in HIR by using FEM, Constr. Build. Mater. 243 (2020) 118304.
[19] X. Ji, Z. Wang, H. Zhang, X. Wang, J. Huo, T. Zhang, Optimization design and characterization of slag cementitious composites containing carbide slag and desulfurized gypsum based on response surface methodology, J. Build. Eng. 77 (2023) 107441.
[20] P. Cong, Y. Cheng, W. Ge, A. Zhang, Mechanical, microstructure and reaction process of calcium carbide slag-waste red brick powder based alkali-activated materials (CWAAMs), J. Clean. Prod. 331 (2022) 129845.
[21] F.A. Cardoso, H.C. Fernandes, R.G. Pileggi, M.A. Cincotto, V.M. John, Carbide lime and industrial hydrated lime characterization, Powder Technol. 195 (2) (2009) 143–149.
[22] J. Cheng, J. Zhou, J. Liu, X. Cao, K. Cen, Physicochemical characterizations and desulfurization properties in coal combustion of three calcium and sodium industrial wastes, Energy & Fuels 23 (5) (2009) 2506–2516.
[23] C. Phetchuay, S. Horpibulsuk, C. Suksiripattanapong, A. Chinkulkijniwat, A. Arulrajah, M.M. Disfani, Calcium carbide residue: alkaline activator for clay–fly ash geopolymer, Constr. Build. Mater. 69 (2014) 285–294.
[24] M. Li, Q. Zhao, C. Li, H. Pan, Optimization design and mechanical properties of multi-component ecological gelling materials, J. Clean. Prod. 443 (2024) 140970.
[25] G. Gu, F. Xu, X. Huang, S. Ruan, C. Peng, J. Lin, Foamed geopolymer: the relationship between rheological properties of geopolymer paste and pore-formation mechanism, J. Clean. Prod. 277 (2020) 123238.

[26] Y. Zhang, Y. Jiang, T.-C. Ling, Use of CO2 as a controlled foam stabilizer to enhance pore structure and properties of foamed concrete, Cement Concr. Compos. 145 (2024) 105356.
[27] D. Zhou, H. Gao, H. Liao, L. Fang, F. Cheng, Enhancing the performance of foam concrete containing fly ash and steel slag via a pressure foaming process, J. Clean. Prod. 329 (2021) 129664.
[28] T.T. Nguyen, H.H. Bui, T.D. Ngo, G.D. Nguyen, Experimental and numerical investigation of influence of air-voids on the compressive behaviour of foamed concrete, Mater. Des. 130 (2017) 103–119.
[29] N. Narayanan, K. Ramamurthy, Structure and properties of aerated concrete: a review, Cement Concr. Compos. 22 (5) (2000) 321–329.
[30] X. Gu, S. Wang, J. Liu, H. Wang, X. Xu, Q. Wang, Z. Zhu, Effect of hydroxypropyl methyl cellulose (HPMC) as foam stabilizer on the workability and pore structure of iron tailings sand autoclaved aerated concrete, Constr. Build. Mater. 376 (2023) 130979.
[31] X. Zhang, K. Wu, Z. Yuan, S. Liu, Investigations into magnesium oxide carbon sequestration foamed concrete: mechanical performance, microstructure and environmental benefits, Constr. Build. Mater. 421 (2024) 135679.
[32] F.K. Alqahtani, M.A. Sherif, A.M. Ghanem, Green lightweight concrete utilizing sustainable processed recycled plastic aggregates: technical, economic and environmental assessment, Constr. Build. Mater. 393 (2023) 132027.
[33] ISO, Environmental Management – Life Cycle Assessment – Principles and Framework ISO 14040:2006, 2006.
[34] P. Van den Heede, A. Mignon, G. Habert, N. De Belie, Cradle-to-gate life cycle assessment of self-healing engineered cementitious composite with in-house developed (semi-)synthetic superabsorbent polymers, Cement Concr. Compos. 94 (2018) 166–180.
[35] C. Li, Y. Li, W. Zhu, G. Zeng, Z. Ouyang, M. Cheng, Z. Jiang, Carbon dioxide cured building materials as an approach to decarbonizing the calcium carbide related industry, Renew. Sustain. Energy Rev. 186 (2023) 113688.
[36] G.V.P. Bhagath Singh, V. Durga Prasad, Environmental impact of concrete containing high volume fly ash and ground granulated blast furnace slag, J. Clean. Prod. 448 (2024) 141729.
[37] W. Li, Y. Yi, Use of carbide slag from acetylene industry for activation of ground granulated blast-furnace slag, Constr. Build. Mater. 238 (2020) 117713.
[38] X. Qian, J. Wang, L. Wang, Y. Fang, P. Chen, M. Li, A clean dispersant for nano-silica to enhance the performance of cement mortars, J. Clean. Prod. 371 (2022) 133647.
[39] G. Kai, C. Yongqiang, D.L. L, W.C. E, In situ quasi-elastic neutron scattering study on the water dynamics and reaction mechanisms in alkali-activated slags, Phys. Chem. Chem. Phys. : Phys. Chem. Chem. Phys. 21 (20) (2019) 10277–10292.
[40] Z. Xu, J. Gao, Y. Zhao, S. Li, Z. Guo, X. Luo, G. Chen, Promoting utilization rate of ground granulated blast furnace slag (GGBS): Incorporation of nanosilica to improve the properties of blended cement containing high volume GGBS, J. Clean. Prod. 332 (2022) 130096.
[41] Z. Jia, C. Chen, H. Zhou, Y. Zhang, The characteristics and formation mechanism of the dark rim in alkali-activated slag, Cement Concr. Compos. 112 (2020) 103682.
[42] J. He, W. Zheng, W. Bai, T. Hu, J. He, X. Song, Effect of reactive MgO on hydration and properties of alkali-activated slag pastes with different activators, Constr. Build. Mater. 271 (2021) 121608.
[43] J.E. Oh, P.J.M. Monteiro, S.S. Jun, S. Choi, S.M. Clark, The evolution of strength and crystalline phases for alkali-activated ground blast furnace slag and fly ash-based geopolymers, Cement Concr. Res. 40 (2) (2010) 189–196.
[44] J. Lyu, S. Feng, Q. Zhang, H. Xiao, Review of factors affecting bond strength between ultra-high-performance concrete and normal strength substrate, Constr. Build. Mater. 439 (2024) 137416.
[45] M.S. Kim, Y. Jun, C. Lee, J.E. Oh, Use of CaO as an activator for producing a price-competitive non-cement structural binder using ground granulated blast furnace slag, Cement Concr. Res. 54 (2013) 208–214.
[46] H. Park, Y. Jeong, Y. Jun, J.-H. Jeong, J.E. Oh, Strength enhancement and pore-size refinement in clinker-free CaO-activated GGBFS systems through substitution with gypsum, Cement Concr. Compos. 68 (2016) 57–65.
[47] A. Schöler, B. Lothenbach, F. Winnefeld, M. Zajac, Hydration of quaternary Portland cement blends containing blast-furnace slag, siliceous fly ash and limestone powder, Cement Concr. Compos. 55 (2015) 374–382.
[48] F. Puertas, M. Palacios, H. Manzano, J.S. Dolado, A. Rico, J. Rodríguez, A model for the C-A-S-H gel formed in alkali-activated slag cements, J. Eur. Ceram. Soc. 31 (12) (2011) 2043–2056.
[49] C. Panagiotopoulou, G. Kakali, S. Tsivilis, T. Perraki, M. Perraki, Synthesis and characterisation of slag based geopolymers, Mater. Sci. Forum 890 (636–637) (2010) 155–160.
[50] L. Zhirong, M.A. Uddin, S. Zhanxue, FT-IR and XRD analysis of natural Na-bentonite and Cu(II)-loaded Na-bentonite, Spectrochim. Acta Mol. Biomol. Spectrosc. 79 (5) (2011) 1013–1016.
[51] H.E. Didamony, A.A. Amer, M. Arif, Impact of Ethylene Glycol Addition on the Physico-Chemical and Mechanical Properties of Alkali Activated GGBFS Pastes, 2015.
[52] L. Fernandez, C. Alonso, A. Hidalgo, C. Andrade, The role of magnesium during the hydration of C3S and C-S-H formation. Scanning electron microscopy and mid-infrared studies, Adv. Cement Res. 17 (1) (2005) 9–21.
[53] M.A. Trezza, A.E. Lavat, Analysis of the system 3CaO·Al2O3–CaSO4·2H2O–CaCO3–H2O by FT-IR spectroscopy, Cement Concr. Res. 31 (6) (2001) 869–872.
[54] T. López, P. Bosch, M. Asomoza, R. Gómez, E. Ramos, DTA-TGA and FTIR spectroscopies of sol-gel hydrotalcites: aluminum source effect on physicochemical properties, Mater. Lett. 31 (3) (1997) 311–316.
[55] A.H. López, J.L.G. Calvo, J.G. Olmo, S. Petit, M.C. Alonso, Microstructural evolution of calcium aluminate cements hydration with silica fume and fly ash additions by scanning electron microscopy, and mid and near-infrared spectroscopy, J. Am. Ceram. Soc. 91 (4) (2008) 1258–1265.
[56] B. Šavija, H. Zhang, E. Schlangen, Influence of microencapsulated phase change material (PCM) addition on (micro) mechanical properties of cement paste, Materials 10 (8) (2017) 863.
[57] N. Jiang, Z. Ge, Z. Wang, T. Gao, H. Zhang, Y. Ling, B. Šavija, Size effect on compressive strength of foamed concrete: experimental and numerical studies, Mater. Des. 240 (2024) 112841.
[58] N. Jiang, Z. Ge, Y. Guan, Z. Zuo, H. Zhang, Y. Ling, B. Šavija, Experimentally validated meso-scale fracture modelling of foamed concrete, Theor. Appl. Fract. Mech. 122 (2022) 103631.
[59] N.Y. Mostafa, Influence of air-cooled slag on physicochemical properties of autoclaved aerated concrete, Cement Concr. Res. 35 (7) (2005) 1349–1357.
[60] E.P. Kearsley, P.J. Wainwright, The effect of porosity on the strength of foamed concrete, Cement Concr. Res. 32 (2) (2002) 233–239.
[61] M.T. Souza, C.K. Maykot, A.C.Z. Araújo, F. Raupp-Pereira, A.P. Novaes de Oliveira, Electrolytes' influence on foamability and foam stability of cement suspensions, Constr. Build. Mater. 157 (2017) 363–371.
[62] H.A. Shah, Q. Yuan, S. Zuo, Air entrainment in fresh concrete and its effects on hardened concrete-a review, Constr. Build. Mater. 274 (2021) 121835.
[63] E.K.K. Nambiar, K. Ramamurthy, Air-void characterisation of foam concrete, Cement Concr. Res. 37 (2) (2007) 221–230.
[64] M. Schmitt, M. Halisch, C. Müller, C.P. Fernandes, Classification and quantification of pore shapes in sandstone reservoir rocks with 3-D X-ray micro-computed tomography, Solid Earth Discussions 7 (4) (2015) 3441–3479.
[65] T. Zingg, Beitrag Zur Schotteranalyse, 1935.
[66] Y. Guo, X. Chen, B. Chen, R. Wen, P. Wu, Analysis of foamed concrete pore structure of railway roadbed based on X-ray computed tomography, Constr. Build. Mater. 273 (2021) 121773.
[67] D. Zhao, J. Xu, Z. Han, Y. Liu, Y. Liu, X. Yang, Study on the correlation between pore structure characterization and early mechanical properties of foamed concrete based on X-CT, Constr. Build. Mater. 450 (2024) 138603.
[68] W. Song, M. Zhang, H. Wu, Gray correlation analysis between mechanical performance and pore characteristics of permeable concrete, J. Build. Eng. 86 (2024) 108793.